Water Resources Research

RESEARCH ARTICLE
10.1029/2018WR024137

Key Points:
- A screening method was employed to study impact of physical and chemical heterogeneity on reaction rates for multimineral rocks
- The proximity of reacted minerals to fast flow pathways is a key determinant of reaction dynamics
- The preferential channeling, as opposed to uniform dissolution, was promoted by a higher degree of physical and/or chemical heterogeneity

Supporting Information:
- Supporting Information S1

Correspondence to:
Q. Lin,
q.lin11@imperial.ac.uk

Citation:
Al-Khulaifi, Y., Lin, Q., Blunt, M. J., & Bijeljic, B. (2019). Pore-scale dissolution by CO_2 saturated brine in a multimineral carbonate at reservoir conditions: Impact of physical and chemical heterogeneity. *Water Resources Research*, *55*, 3171–3193. https://doi.org/10.1029/2018WR024137

Received 19 SEP 2018
Accepted 10 FEB 2019
Accepted article online 19 FEB 2019
Published online 18 APR 2019

©2019. The Authors.
This is an open access article under the terms of the Creative Commons Attribution-NonCommercial-NoDerivs License, which permits use and distribution in any medium, provided the original work is properly cited, the use is non-commercial and no modifications or adaptations are made.

Pore-Scale Dissolution by CO_2 Saturated Brine in a Multimineral Carbonate at Reservoir Conditions: Impact of Physical and Chemical Heterogeneity

Yousef Al-Khulaifi[1,2], Qingyang Lin[1], Martin J. Blunt[1,2], and Branko Bijeljic[1,2]

[1]Department of Earth Science and Engineering, Imperial College London, London, UK, [2]Qatar Carbonates and Carbon Storage Research Centre, Department of Earth Science and Engineering, Imperial College London, London, UK

Abstract We study the impact of physical and chemical heterogeneity on reaction rates in multimineral porous media. We selected two pairs of carbonate samples of different physical heterogeneity in accordance with their initial computed velocity distributions and then injected CO_2 saturated brine at reservoir conditions at two flow rates. We periodically imaged the samples using X-ray microtomography. The mineralogical composition was similar (a ratio of dolomite to calcite of 8:1), but the intrinsic reaction rates and mineral spatial distribution were profoundly different. Visualizations of velocity fields and reacted mineral distributions revealed that a dominant flow channel formed in all cases. The more physically homogeneous samples had a narrower velocity distribution and more preexisting fast channels, which promoted dominant channel formation in their proximity. In contrast, the heterogeneous samples exhibit a broader distribution of velocities and fewer fast channels, which accentuated nonuniform calcite distribution and favored calcite dissolution away from the initially fast pathways. We quantify the impact of physical and chemical heterogeneity by computing the proximity of reacted minerals to the fast flow pathways. The average reaction rates were an order of magnitude lower than the intrinsic ones due to mass transfer limitations. The effective reaction rate of calcite decreased by an order of magnitude, in both fast channels and slow regions. After channel formation calcite was shielded by dolomite whose effective rate in slow regions could even increase. Overall, the preferential channeling effect, as opposed to uniform dissolution, was promoted by a higher degree of physical and/or chemical heterogeneity.

1. Introduction

Carbon capture and storage is a viable option to mitigate atmospheric CO_2 emissions (Bachu, 2000). The largest identified storage potential sites are deep saline aquifers (Celia et al., 2015). The injection of CO_2 into geologic aquifers acidifies the in situ brine (Peng et al., 2013) and leads to the partial dissolution of carbonate bearing host rocks (Morse & Mackenzie, 1990). The physical changes in pore structure resulting from the flow of reactive brine are of great interest since they have direct impact on alteration of flow properties and storage capacity (Metz et al., 2005). To ensure storage security, modeling of these subsurface processes is important (Sifuentes et al., 2009). However, field-scale models require a pore-scale understanding of the reaction processes to account for complexities inherent in carbonate reservoirs (Li et al., 2006, 2008; Steefel, Appelo, et al., 2015; Steefel, Beckingham & Landrot 2015; Steefel & Lasaga, 1994; Steefel & Maher, 2009). These reactive processes are dependent on pore structure (physical heterogeneity) and rock mineralogy (chemical heterogeneity). Although in single-mineral rock it has been observed that initial pore structure and fluid/solid reactivity play a part in dictating the type of dissolution that will take place (Al-Khulaifi et al., 2017, 2018; Li et al., 2014; Menke et al., 2017), the more complex physicochemical couplings in chemically heterogeneous media are not fully understood. Hence, investigating the impact of physical and chemical heterogeneity at different flow rates in chemically heterogeneous rock is the main goal of our study.

The discrepancy between field and laboratory dissolution rate of minerals is one of the challenges posed in modeling (Li et al., 2006; Moore et al., 2012; Noiriel et al., 2004; Swoboda-Colberg & Drever, 1993; White & Brantley, 2003). Early empirical comparison attributed this mismatch to the incomplete contact between rock minerals and the flowing acidic solution. Salehikhoo and Li (2015) found that by using an effective

surface area of mineral in contact with reactant, as opposed to the total BET (Brunauer–Emmett–Teller) surface area, they were able to arrive at a very close match between lab measured and field rates. Initial pore structure can dictate the type of dissolution, ranging from uniform to preferential channel growth, which limits dissolution to a single or only a few channels (Al-Khulaifi et al., 2018; Menke et al., 2016). Dissolution patterns also have a direct impact on how permeability changes with increasing porosity (Al-Khulaifi et al., 2018; Hao et al., 2013; Luquot & Gouze, 2009; Menke et al., 2016; Noiriel et al., 2004; Smith et al., 2013). Because of this strong dependence on how rock properties impact dissolution patterns, it is important to be able to predict them. Recent reactive core flood experiments in single-mineral carbonates have shown nonuniform dissolution at the reactive transport conditions that would normally describe a uniform dissolution regime in homogeneous materials, thus pointing out to the importance of impact of physical heterogeneity on reaction (Al-Khulaifi et al., 2017, 2018; Menke et al., 2016, 2018).

However, in multimineral carbonates, a wide range of reaction rates is possible which means that they can be harder to predict (Black et al., 2015). There have been benchmark studies that attempt to model multicomponent reactive transport; most report the need for experimental validation and all agree on anchoring the fundamental chemical and physical processes from pore-scale observations (Beisman et al., 2015; Li et al., 2006; Marty et al., 2015; Molins et al., 2012; Steefel, Appelo, et al., 2015; Steefel, Beckingham, & Landrot, 2015; Steefel & Lasaga, 1994).

X-ray microtomography is a powerful method to study the pore-scale changes induced by rock dissolution (Al-Khulaifi et al., 2017, 2018; Gharbi et al., 2013; Gouze & Luquot, 2011; Luquot & Gouze, 2009; Menke et al., 2015, 2016; Noiriel et al., 2004, 2005, 2009). Rock property alterations resulting from dissolution depend on the spatial distribution of minerals (mineral heterogeneity), pore structure, reservoir conditions, and flow/transport conditions (Al-Khulaifi et al., 2017, 2018; Noiriel et al., 2005; Wang et al., 1993). There are many laboratory observations on single mineral dissolution by CO_2 acidified formation brine under varying transport conditions (Al-Khulaifi et al., 2018; Gharbi et al., 2013; Gouze & Luquot, 2011; Luquot & Gouze, 2009; Menke et al., 2015, 2016, 2017, 2018; Noiriel et al., 2004, 2005). It has been shown that even in single mineral systems, reaction rates and the dissolution pattern depend strongly on the initial pore structure of the reactive medium and flow rate (Al-Khulaifi et al., 2018; Maheshwari et al., 2013; Menke et al., 2016; Smith et al., 2017). Al-Khulaifi et al. (2018) have demonstrated that increased initial pore structure heterogeneity (and thus flow heterogeneity) in dolomite leads to more unstable dissolution fronts at low flow rates (Péclet numbers, Pe, in the range 420–360), which in turn causes the reaction rate to decrease (due to dissolution becoming spatially limited to a channel) and the permeability-porosity relationship to exhibit a stronger dependency (permeability increases more sharply with porosity change). However, at high flow rates (Pe = 2,650–1,630), dissolution was more uniform and not dependent on the initial flow heterogeneity.

The findings from studying single mineral systems are important, but the norm in geologic sites is a heterogeneous spatial distribution of minerals (Li et al., 2014). An exemplar study of CO_2-saturated brine injection in a mixed-mineralogy system composed of dolomite and calcite arranged in series was performed to assess how the evolution of pore structure and flow field induced by dissolution in dolomite would affect that in calcite (Al-Khulaifi et al., 2017). This dolomite/calcite system was designed to have sharply contrasting initial pore structure/flow/transport heterogeneity and intrinsic reaction rates. The study demonstrated how dynamic changes in the flow field heterogeneity in dolomite can profoundly change the dissolution pattern in calcite. However, the spatial distribution of minerals was uniform with two mineralogically homogeneous samples placed together. In this study we will perform experiments on natural mixed mineralogy samples consisting of calcite and dolomite that are nonuniformly distributed.

Several studies have investigated dissolution in natural multimineral systems at the centimeter scale. Smith et al. (2014) performed reactive flow experiments in carbonate reservoir core plugs made from a mix of calcite and dolomite and continuously measured the pressure drop under constant flow to assess permeability changes while simultaneously performing X-ray imaging at 42.5 micron resolution. They observed that despite the low content of calcite in the overall sample composition, its dissolution had a dominating effect on permeability changes. Smith et al. (2014) highlighted the importance of higher resolution observations to evaluate porosity-permeability relationships in mixed-mineralogy systems; this will be one of the aims of our study. Ellis et al. (2011) injected CO_2-acidified brine through a carbonate caprock at reservoir conditions and

reported a preferential dissolution of calcite over dolomite. They observed that the evolution of permeability depends in a complex way on the heterogeneity of the carbonate minerals and their spatial pattern. Salehikhoo and Li (2015) examined how mineral dissolution rates are affected by their spatial distribution and suggested that the difference in the rates between laboratory and field scales could be in part caused by the spatial distributions of minerals.

Previous experimental studies provide evidence that the spatial distribution of minerals with different intrinsic reaction rates, different pore structure/connectivity, and associated flow/transport heterogeneities can contribute to the complexity of dissolution in natural systems. This leads to the question of how to differentiate the impact of pore structure, flow, and transport from spatially nonuniform reaction rate effects, which act simultaneously during dissolution. To address this, we use a combined experimental and numerical simulation approach that examines dissolution in a naturally heterogeneous rock containing dolomite and calcite distributed nonuniformly in space. Our approach consists of screening the rock samples to obtain two pairs of samples with similar physical heterogeneity defined by the velocity distribution obtained using direct numerical simulation. For each heterogeneity pair, we inject CO_2 saturated brine at reservoir conditions at two flow rates to examine the impact of transport conditions. Finally, we analyze transport and reaction parameters and show that effective reaction rates and dissolution patterns behavior can be accurately described by examining proximity of minerals to fast channels and slow regions through the use of reacted mineral distributions.

2. Materials and Methods

2.1. Reservoir Carbonate Samples

The carbonate chosen for this study comes from an underground aquifer in the Middle East. X-ray diffraction analysis shows that the sample is 86.6% dolomite and 11.1% calcite, with an average porosity of 0.109 measured from helium porosimetry on a 3.8- by 7.6-cm core plug. A petrographic analysis revealed a dolomitised matrix with calcite micritic envelopes. It is a dolopackstone that is bimodal in dolomite crystal size with very fine to aphano-crystalline grains. For our experiments, all the core samples used were 5-mm diameter by 5-mm length drilled parallel to the plane of bedding. Initially, we performed low-energy (50 KeV) dry scans to maximize the image contrast so that we were able to differentiate between dolomite and calcite mineral. Figure 1 shows a gray-scale image of a representative sample where calcite, dolomite, and void space are easily distinguishable. The image size was $1{,}000^3$ voxels with 5.2-μm voxel size, which provided a field of view spanning the entire core.

The initial distribution of calcite within each sample was nonuniform in both location and size, which makes it chemically heterogeneous. As we will show later in section 2.4, initial velocity distributions of the four carbonate samples selected for our study show distinct ranges of values indicating two pairs of samples having different physical (flow) heterogeneity.

2.2. Experimental Methodology and the SPIM Method

The screening process (see supporting information) involved coring ten 5-mm length by 5-mm diameter samples from a larger piece of rock; the length of the cores extracted was parallel to the bedding plane. Dry scans of these 10 samples were taken to assess their pore structure heterogeneity. This was done by implementing a flow simulator (details in section 2.4) directly on the segmented image pore space from which the pore velocity distributions were compared to find matching pairs. Two pairs of samples A and B with similar flow characteristics were chosen for experimentation applying this method. We term it the Screening for Pore-scale Imaging and Modeling (SPIM) method (Al-Khulaifi et al., 2018).

The experiment was conducted by injecting supercritical CO_2 ($scCO_2$) acidified brine in each of the four samples; within each pair of matching sample heterogeneity, there was a high flow rate (0.5 ml/min—with Pe ~ 1,000, see Table 1) and a low flow rate (0.1 ml/min—with Pe ~ 100) experiment, which we label H and L, respectively. A single layer of aluminum foil tape was wrapped around the length of each core, leaving the ends open, to prevent CO_2 gas from leaking out laterally during the acidic-brine flood. The sample was wrapped with a layer of aluminum to prevent CO_2 leakage and then inserted into a Viton sleeve. This assembly was inserted into a Hassler type core holder made of carbon fiber where it was to be confined with an overburden pressure of 2 MPa at all times by a separate deionized water pump. The carbon fiber sleeve was wrapped in

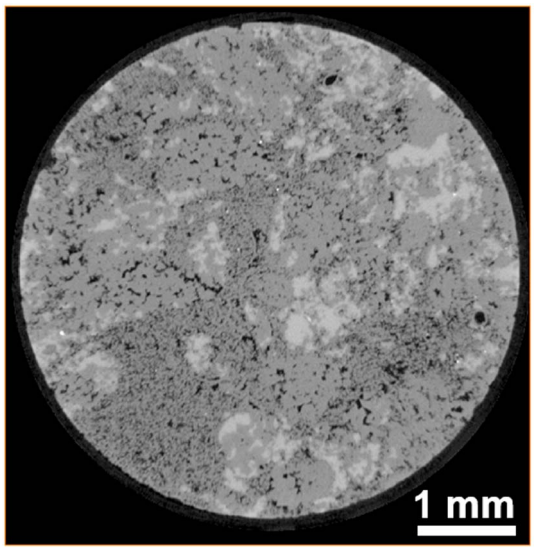

Figure 1. A 2-D cross section of a 3-D 50-KeV dry scan of a sample imaged with a 5.2-μm voxel size. Low-energy scans give sufficient image contrast to differentiate between pore (black), dolomite (gray), and calcite (white).

a heating tape, which maintained the core at 50 °C using a thermocouple that measured temperature at the rock sample. Figures 2 and 3 show a schematic of the core holder assembly and the experimental apparatus.

Next, CO_2 was pumped into a sealed reactor, which had been partially prefilled with brine, to a pressure of 10 MPa. A heating jacket brought the contents of the reactor up to a temperature of 50 °C and these conditions were maintained overnight to ensure full equilibration of the supercritical, $scCO_2$ with the brine. A mixer continuously stirred the contents of the reactor to help maintain full equilibration. After the core holder was connected to the flow system and installed on the rotation stage, 6% KI (Potassium iodide) doped brine was back flowed via the receiving pump to wet the core and purge the flow lines of air. Once a steady flow of the KI brine solution was established through the three-way valve at the outlet of the reactor, this valve was closed and the receiving pump gradually brought the core up to a pressure of 10 MPa while constantly maintaining a 2 MPa overburden pressure from the confining fluid. A heating tape wrapped around the carbon fiber sleeve maintained the core temperature at 50 °C. Next, the reactive brine was introduced into the system and the receiving pump was set to refill at the desired flow rate to initiate the flow of acid. At this point, projections of the core sample were monitored for the arrival of the reactive brine that was signaled when the X-ray attenuating through the sample. At this precise moment, the series of consecutive scans were started and changes in the pore structure due to dissolution were imaged in situ for the duration of the core flood. The number of pore volumes (PV) injected was calculated between two consecutive scans as $\mathrm{PV}_{n,n+1} = \frac{Q\Delta t_{n,n+1}}{V_{\mathrm{bulk}}\phi_n}$, where Q is the flow rate, $\Delta t_{n,n+1}$ is the time period between two scans equaling 33 min, V_{bulk} is the bulk volume of the sample, and ϕ_n is the connected porosity at scan n.

In our experiments, the acidic brine pH at reservoir conditions remained largely unchanged since the core was too short to see any measurable buffering effect.

2.3. Reaction Rate, Péclet, and Damköhler Number

We denote u_{avg} as the average pore velocity calculated by dividing the Darcy velocity by the segmented image calculated porosity (ϕ_{CT}). The Péclet number (Pe) can be estimated by comparing the rate of mass transport of the solute by advection to that by diffusion:

$$\mathrm{Pe} = \frac{\text{advective transport rate}}{\text{diffusive transport rate}} = \frac{u_{\mathrm{avg}} L_c}{D_m} \tag{1}$$

D_m is molecular diffusion coefficient; here we use 7.5×10^{-10} m^2/s for Ca^{2+} at 25 °C from Luquot and Gouze (2009), and L_c is a characteristic length in meters calculated by $L_c = \pi/S$ (Mostaghimi et al. 2012)

Table 1
The Average Reaction Rates for Calcite and Dolomite Samples with Heterogeneities A and B at the High and Low Flow Rates Calculated Over the Full Course of the Experiments

Sample	AL	AH	BL	BH
Calcite average r_{eff} (mol/m^2s)	5.08×10^{-6}	5.45×10^{-6}	1.09×10^{-5}	3.42×10^{-6}
Dolomite average r_{eff} (mol/m^2s)	1.23×10^{-6}	2.69×10^{-6}	9.80×10^{-7}	3.21×10^{-6}
Initial Pe	212	1,030	164	1,746
Final Pe	126	529	109	642
Calcite initial Da	1.11×10^{-3}	2.13×10^{-4}	1.08×10^{-3}	2.28×10^{-4}
Calcite final Da	1.83×10^{-3}	4.69×10^{-4}	1.88×10^{-3}	6.22×10^{-4}
Dolomite initial Da	1.32×10^{-5}	3.11×10^{-6}	1.87×10^{-5}	2.20×10^{-6}
Dolomite final Da	2.05×10^{-5}	3.11×10^{-6}	2.61×10^{-5}	5.27×10^{-6}

Note. Initial and final values for Pe and Da numbers for calcite and dolomite are also shown.

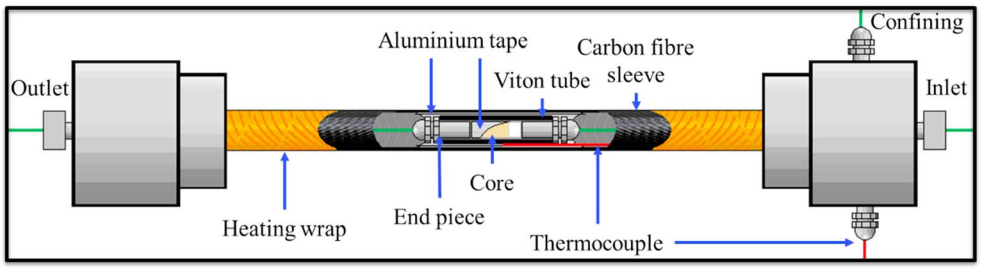

Figure 2. X-ray transparent carbon fiber Hassler type core holder assembly. The design used flexible PEEK (Polyaryletheretherketone) tubing that allows the core holder to rotate with the micro-CT stage during image acquisition.

where the specific surface area S (m^{-1}) is the ratio of bulk volume (V_B) to surface area A_s from image analysis.

We report Damköhler numbers for calcite and dolomite since in multimineral applications the samples contain minerals that dissolve at different intrinsic reaction rates. A common form of the Damköhler number is the ratio of the reaction rate to mass transport through advection:

$$\mathrm{Da} = \frac{\text{reaction rate}}{\text{advective transport rate}} = \frac{L_c}{u_{\mathrm{avg}}} k \tag{2}$$

where k is the chemical reaction rate constant (s^{-1}). If we assume that the mineral grains forming the core sample are spherical, then the reaction rate constant can be estimated using $k = \pi r/nL$ where r is the mineral reaction rate with units of moles/(m^2s), L is the core sample length, and n is the moles of mineral per unit rock volume (Menke et al., 2015):

$$n = \frac{\rho_{\mathrm{mineral}} f_{\mathrm{mineral}}}{M_{\mathrm{mineral}}} \tag{3}$$

ρ_{mineral} is the mineral density (2,820 kg/m^3 for dolomite and 2,710 kg/m^3 for calcite), M_{mineral} is their molecular mass (0.1844 kg/mol for dolomite and 0.1001 kg/mol for calcite), and f_{mineral} is the dolomite or calcite mineral fraction in the total sample bulk volume. Using the above estimate of reaction rate constant, equation (2) can be rewritten in the following manner (Al-Khulaifi et al., 2018):

$$\mathrm{Da} = \frac{\pi r_{\mathrm{mineral}}}{u_{\mathrm{avg}} n} \tag{4}$$

r_{mineral} is the intrinsic (nontransport limited) reaction rate of each mineral measured from batch reaction experiments at the same reservoir conditions as in our experiments: 5.1×10^{-5} mol/m^2 s for dolomite and 8.1×10^{-4} mol/m^2 s for calcite (Peng et al., 2015; Peng et al., 2016). Damköhler numbers were calculated in relation to both dolomite and calcite minerals individually using equation (4). The effective reaction rate (r_{eff}) of calcite and dolomite during dissolution was calculated from mineral volume changes observed between consecutive segmented micro-CT images:

$$r_{\mathrm{eff}} = \frac{\rho_{\mathrm{mineral}} \Delta f_{\mathrm{mineral}}}{M_{\mathrm{mineral}} S \Delta t} \tag{5}$$

where $\Delta f_{\mathrm{mineral}}$ is change in mineral fraction between image scans and Δt is the time between scans. There can be additional dissolution caused by the reactive brine invading the microporosity through diffusion, but this was not observed from imaging as there was no detectable change in the gray scale of the rock grains. We also calculate effective rates of dolomite and calcite separately for fast channels and slow pore regions. This is

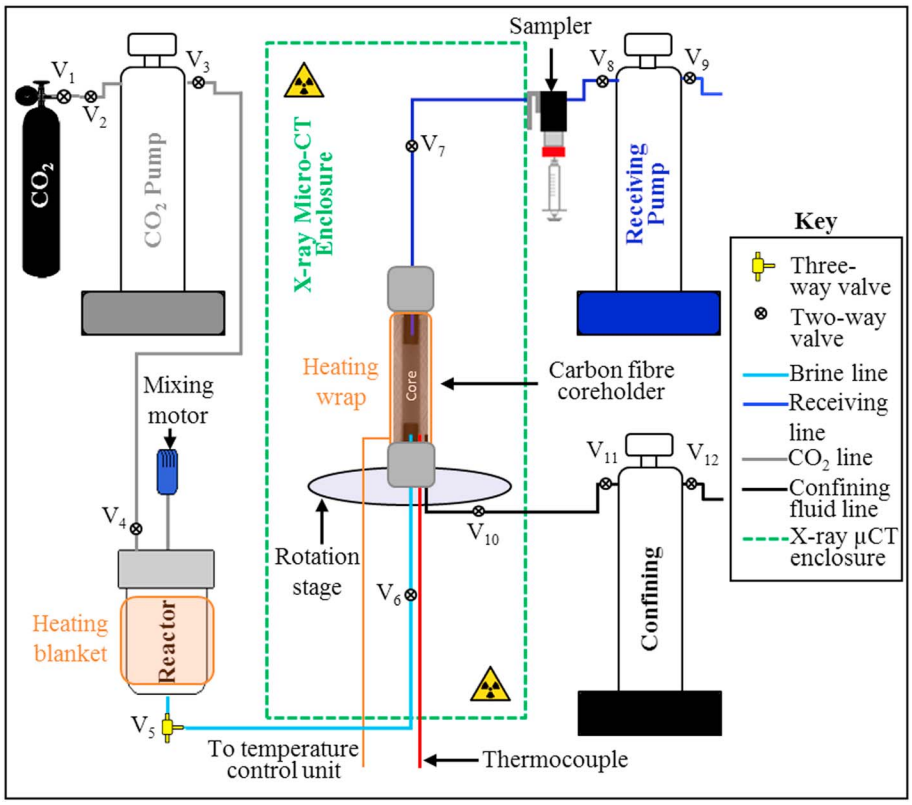

Figure 3. Experimental apparatus schematic showing the flow loop, which consisted of three pumps, a reactor, and a carbon fiber core holder that sat inside the confines of a micro-CT enclosure for in situ imaging.

done using equation (5) in which dissolved voxels of dolomite and calcite in contact with fast and slow regions are counted for the specific surface area calculation.

2.4. Sample Heterogeneity Characterization Based on Flow Modelling

We performed simulations on the segmented pore space using a finite volume solver implemented in OpenFOAM that solves the Navier-Stokes and volume conservation equations simultaneously (Bijeljic, Mostahimi, & Blunt 2013; Raeini et al., 2012):

$$\nabla \cdot u = 0 \tag{6}$$

$$\rho\left(\frac{\partial u}{\partial t} + u \cdot \nabla u\right) = -\nabla p + \mu \nabla^2 u \tag{7}$$

Here p is the pressure and u is the velocity calculated in each pore voxel. μ is the viscosity of water ($\mu = 0.001$ Pa s) and ρ is its density ($\rho = 1{,}000$ kg/m^3) at standard ambient conditions. The resolution of the mesh matches the voxel size of the images. The flow rate was calculated as $Q = \int u_x \, dA_x$ where Q is in cubic meters per second, u_x is the face velocity parallel to flow in meters per second, and A_x is the cross-sectional area of the core perpendicular to the flow direction in square meters. The Darcy velocity was calculated as $u_D = Q/(L_y L_z)$ where L_y and L_z are lengths in the y and z direction of the 3-D image. We calculated the permeability K (m^2) using the Darcy law:

$$K = -\mu \frac{u_D}{\nabla p} \tag{8}$$

where∇p (Pa) was the computed pressure gradient across the core.

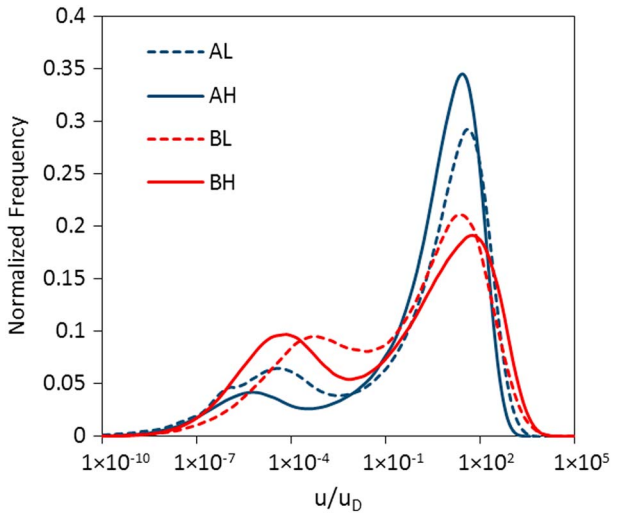

Figure 4. Initial velocity distributions of the reservoir samples. There were two types of heterogeneity, one for each sample pair. A had the less heterogeneous pore structure and B the more heterogeneous pore structure. L and H refer to low and high flow rate experiments respectively.

From the simulations we obtained voxel velocities u and then calculated their probability density functions (PDFs) for each image by sampling them uniformly in bins of $\log(|u|/u_D)$; the shape of the velocity distributions was used to characterize the physical heterogeneity (Bijeljic, Raeini, et al., 2013; Bijeljic, Mostaghimi, & Blunt, 2013). Figure 4 shows the velocity distributions of the initial unreacted state of the four core samples. We grouped them into two pairs with similar velocity distributions: the two more homogeneous distributions (A) had both larger peaks around the Darcy velocity and fewer slow velocities, than the characteristic distributions of the two more heterogeneous samples (B). The characterization of all ten reservoir samples is provided in supporting information.

To relate the impact of transport heterogeneity to mineral spatial heterogeneity, we quantified the proximity of minerals to fast channels and slow regions. The step by step algorithm for our method is provided in Appendix A. The first stage was to discriminate between fast channels and slow regions within each image, using a thresholding method based on labeling those voxels with the highest 25% of velocities in the flow field as belonging to in the fast channels. Once the spatial coordinates of the fast voxels in all fast channels was established, we used them as seeds that were grown in all directions sequentially until the nearest solid wall was encountered. Note that a fast channel will also contain voxel velocities that are in the low velocity range near the walls.

The second stage is to find the proximity of each solid voxel of calcite and dolomite to the fast channels and slow regions. We compute the shortest distance from each solid voxel to the nearest fast channel or slow region of the pore space. In the analysis that follows we study this distance for those mineral voxels that dissolve during the experiment.

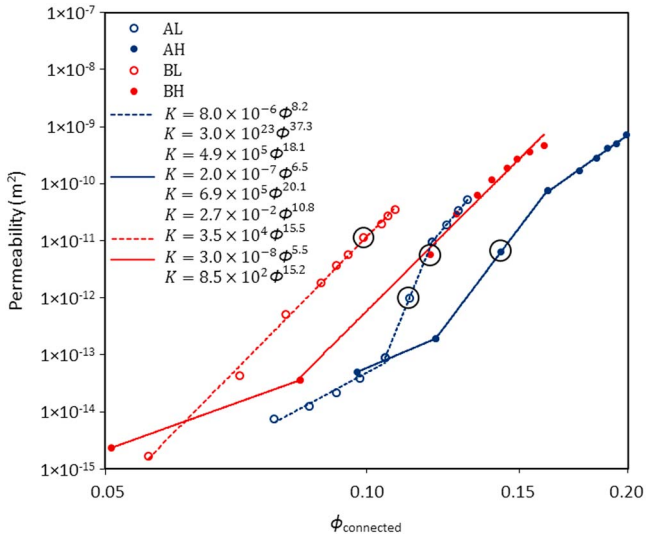

Figure 5. The permeability as a function of connected image porosity calculated from flow simulation. Power law trends are fitted to linear sections of the plots. As dissolution proceeds the porosity-permeability increase is dependent on the channel pattern. The encircled points correspond to the porosities and permeabilities for the first experimental scans following the formation of single preferential channels.

3. Results

In section 3.1 we study dynamic changes in physical heterogeneity. Furthermore, in section 3.2 we analyze dynamic changes in chemical heterogeneity parameters, namely, in mineralogical content, the effective reaction rates and reacted mineral distribution. Finally, in section 3.3, we evaluate the combined impact of chemical and physical (flow) heterogeneity on dissolution dynamics by examining evolution of reacted mineral proximity to fast flow channels and slow regions. A summary of the key observations is provided in Tables B1 and B2 in Appendix B.

3.1. Transport Metrics

3.1.1. Porosity-Permeability Relationship

The time-dependent porosity-permeability relationship for the four cores is plotted in Figure 5. Permeability is obtained by running the Navier-Stokes solver described in section 2.4 on the micro-CT images during dissolution and is plotted against connected porosity.

A power law with the equation $K = c\phi^m_{\text{connected}}$, where K is the permeability (m^2), c is a constant (m^2), m is the power law exponent, and $\phi_{\text{connected}}$ is porosity connected in the direction of flow determined from micro-CT images, is used to fit the porosity-permeability relationships. Previous studies have indicated a broad range of exponents with values of m in the range 0.29–28.3 (Al-Khulaifi et al., 2017, 2018; Luquot & Gouze, 2009; Menke et al., 2016; Noiriel et al., 2004; Smith et al., 2017). The exponents obtained in this study are found to be in the upper range and higher than found previously, since, as discussed in the next section, dissolution

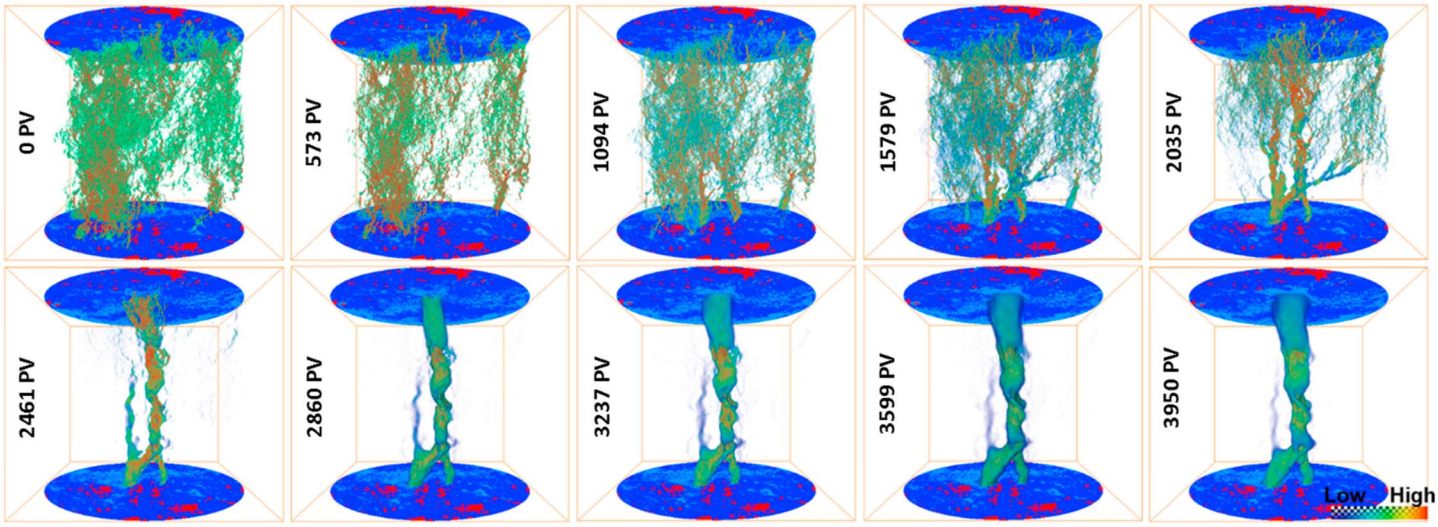

Figure 6. Time lapsed velocity fields for sample AL labeled with the number of pore volumes, PV, injected.

proceeds with the formation of a single channel that occupies only a small fraction of the sample yet completely dominates the permeability, such that a tiny increase in porosity can lead to a huge leap in permeability. This is seen in Figure 5 for A samples from the encircled points representing the porosities and permeabilities for the first experimental scans taken after the formation of single preferential channel. This is the point at which the preexisting channels in more homogeneous samples A merged into the single preferential channel, producing a sharp increase in permeability with a relatively small change in porosity. After the channel is formed there is less reaction which is manifested in a lower exponent.

In a previously published study (Al-Khulaifi et al., 2018), the impact of initial flow heterogeneity was found to be very important. However, for single mineral dissolution, the porosity-permeability relationship for chemically heterogeneous samples studied here additionally depends on the initial distribution of minerals.

3.1.2. Analysis of the Velocity Fields

Figures 6–9 show visualizations of the three-dimensional velocity fields for the four carbonate samples studied. A striking feature that occurs in all four cases is the development of a single channel through which

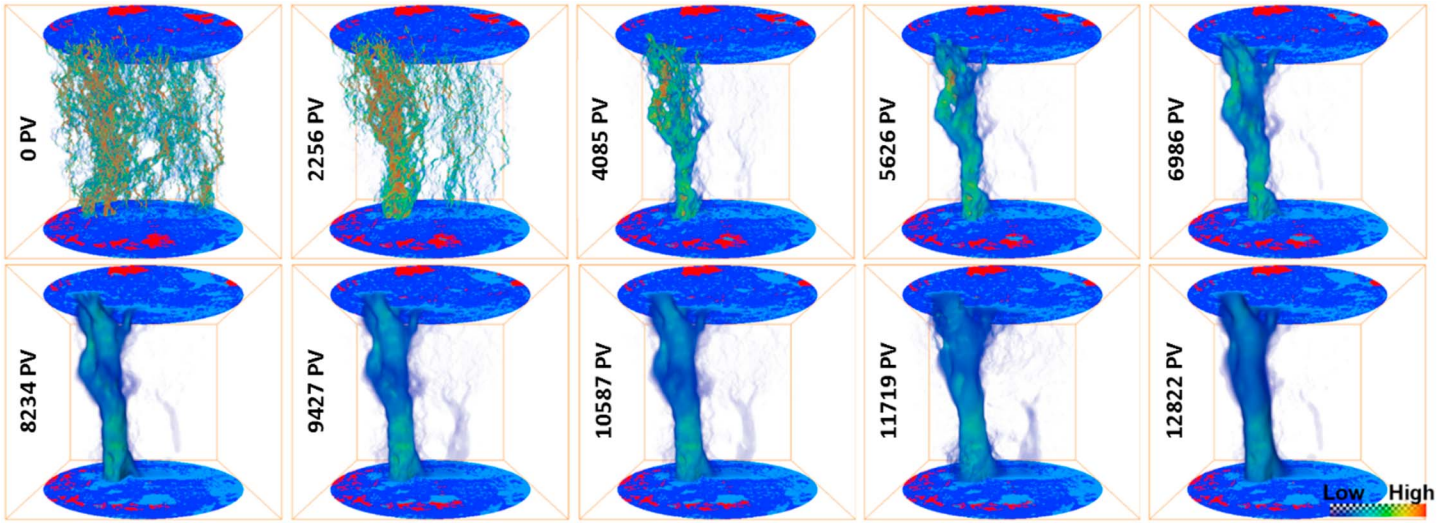

Figure 7. Time lapsed velocity fields for sample AH labeled with the number of pore volumes, PV, injected.

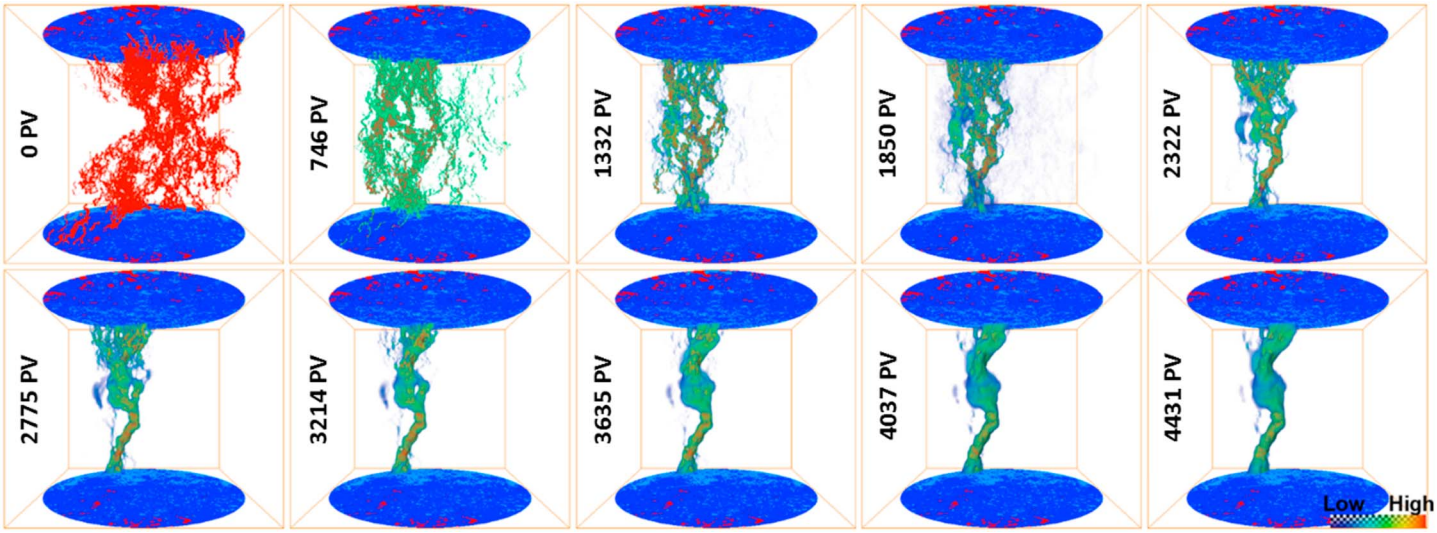

Figure 8. Time lapsed velocity fields for sample BL labeled with the number of pore volumes, PV, injected.

most of the flow streamlines are focused. This has a profound effect on the later-stage dissolution, since most of the mineral volume is at this time away from the single channel and will not be available to the injected reactant, thus resulting in a considerable decrease of the effective reaction rate, as quantified later in section 3.2.2.

The number of pore volumes injected, PV, needed to form single channel is provided in Table B2 in Appendix B. It takes more injected PV to form the single dominant channel at high flow rates since there are more competing channels. The impact of initial flow field heterogeneity can be observed in the early stages of dissolution. Initially, in the A samples, many fast flow channels exist. Calcite and dolomite dissolve and widen these channels, until one of them wins and flow becomes focused. However, in the B samples there are initially fewer fast flow channels throughout the core volume, which makes it more probable that more reactive calcite will be further away from them. Hence, the single channel will not necessarily be formed through one of the initially fast flow channels. In this case chemical heterogeneity, specifically the location of calcite, may determine the final location of the dominant channel. A study on fracture evolution in multimineral systems by Deng et al. (2018) pointed out the role of flow regimes. If the flow rate is reduced

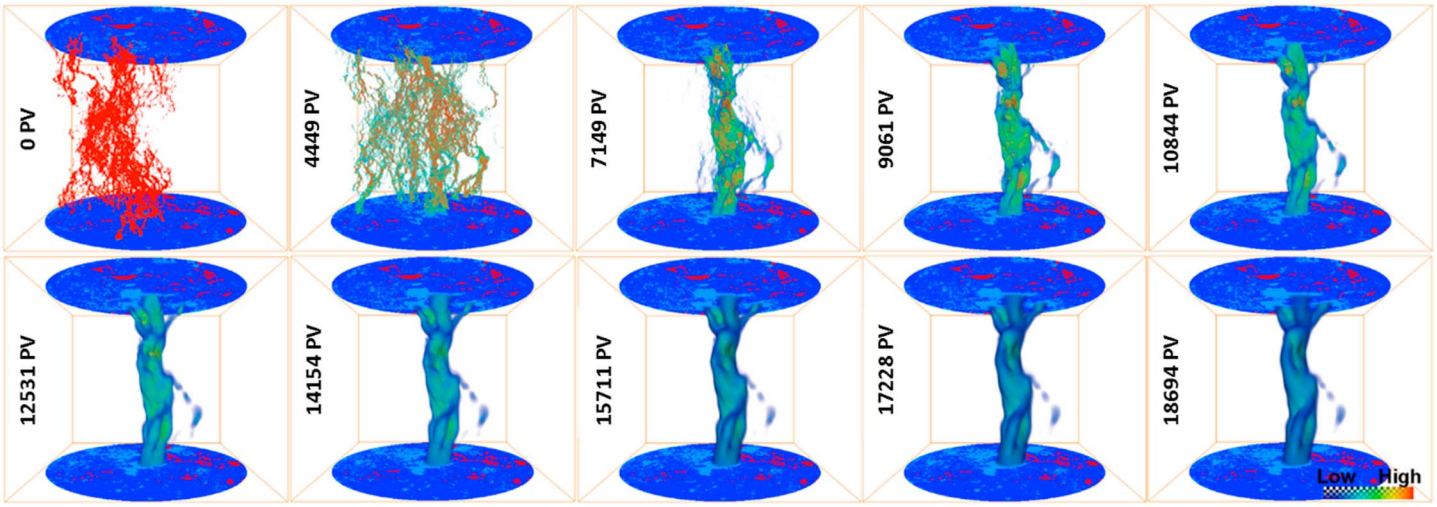

Figure 9. Time lapsed velocity fields for sample BH labeled with the number of pore volumes, PV, injected.

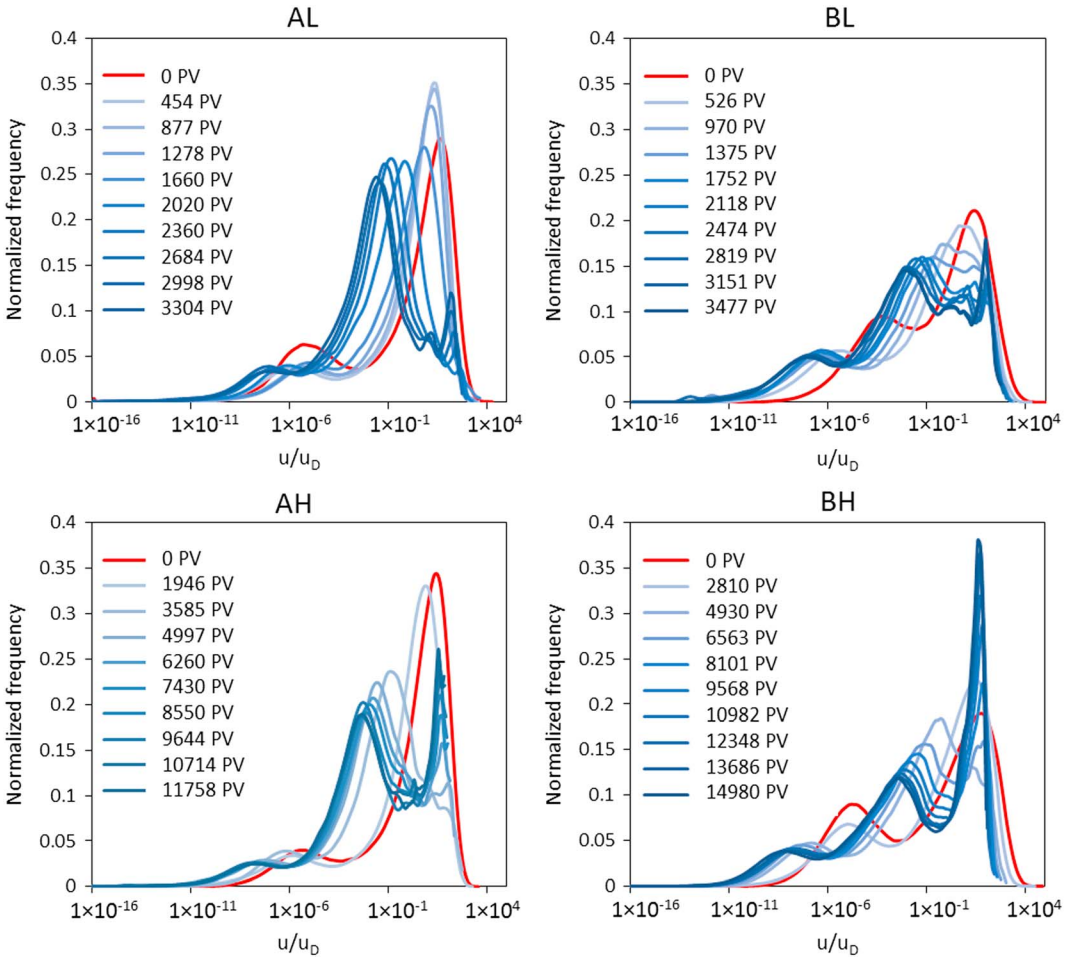

Figure 10. Evolution of probability density functions of velocity for the four samples.

such that calcite dissolution is limited at the inlet and/or calcite is initially away from fast flow channels, dolomite dissolution may become the controlling process for channeling. In this case, channeling in the more heterogeneous samples may again follow the initial fast flow pathway.

3.1.3. Velocity Distributions

The velocity distributions reveal the relative importance of fast flow channels compared to stagnant velocity regions. In Figure 10, time-evolving PDFs of velocities are shown for the four samples.

For all four samples we observe the formation of a secondary peak when the single channel is formed at the later stages of dissolution. As dissolution proceeds, the peaks representing fast and slow regions both shift to the left, indicating that their mode velocities decrease. This is simply because the porosity increases and, at a fixed Darcy flow rate, the average interstitial velocity decreases.

Here we observe the differences related to the two flow rates studied: the secondary peaks for the higher flow rates are more pronounced for both A and B, since the single channels have become wider than in the lower flow rate cases. Correspondingly, less of the initially high velocities become more stagnant relative to the secondary peak.

Overall, the porosity-permeability relationship, velocity fields and velocity distributions can be used to explain the impact of physical heterogeneity at different flow rates on reactive transport. However, in chemically heterogeneous rocks with a nonuniform spatial distribution of minerals having different batch reaction rates, additional analysis needs to be employed, to study the effective reaction rates and evolving spatial distribution of minerals.

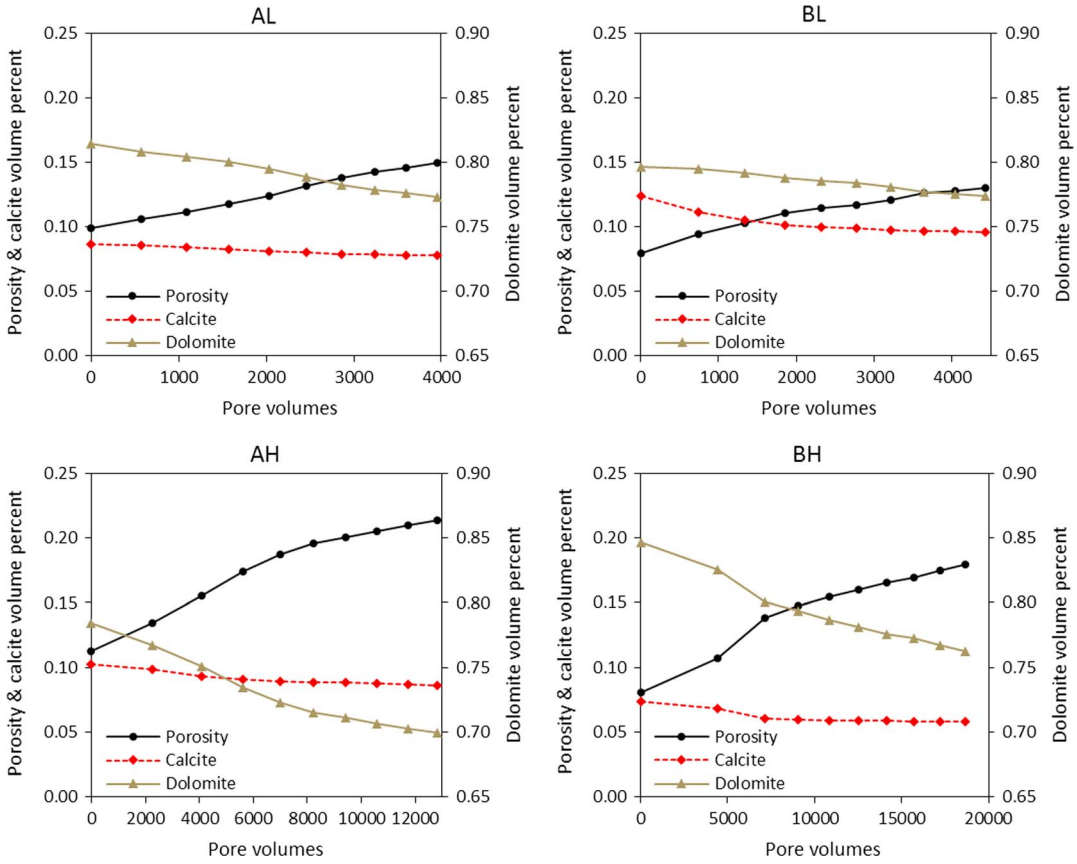

Figure 11. Evolution of porosity and the associated calcite and dolomite volume percent change as a function of pore volumes injected. For better visualization, the dolomite trend is plotted on the secondary axis due to its higher range of values.

3.2. Reaction Metrics

3.2.1. Mineral Volume Changes

The porosity and mineral volume changes during dissolution are shown in Figure 11. The porosity increase after 4,000 pore volumes injected is larger at low flow rate for samples with heterogeneity B. This is because at high flow rates a considerable amount of reactant goes through the system without reacting. This is echoed in initially a more rapid decrease in mineral volume of both calcite and dolomite. For heterogeneity A samples no appreciable difference in porosity increase was observed for different flowrates after the same period of injection.

3.2.2. Effective Reaction Rates

The average reaction rates found from the changes in mineral volume at the end of the experiments are given in Table 1. The intrinsic (batch) reaction rate at the same experimental conditions for calcite is 8.1×10^{-4} mol/m^2 s and for dolomite is 5.1×10^{-5} mol/m^2 s. In all four cases the average reaction rates were at least an order of magnitude lower than the intrinsic reaction rates due to the effect of mass transport limitations to the solid surface in the highly irregular carbonate pore space.

Furthermore, it is important to determine dynamic changes in the effective reaction rates. Figure 12 shows the effective reaction rates for calcite and dolomite as a function of time for the four experiments calculated from the images using equation (5). To assess the impact of flow heterogeneity, we present the effective reaction rates for the full core, fast channels, and slow regions. We also plot the vertical lines representing the number of PV after which the single channel is formed.

The dynamics of the effective reaction rates was different in calcite compared to dolomite. There was a faster decrease in the calcite effective reaction rate for the lower flow rate experiments for both heterogeneities A

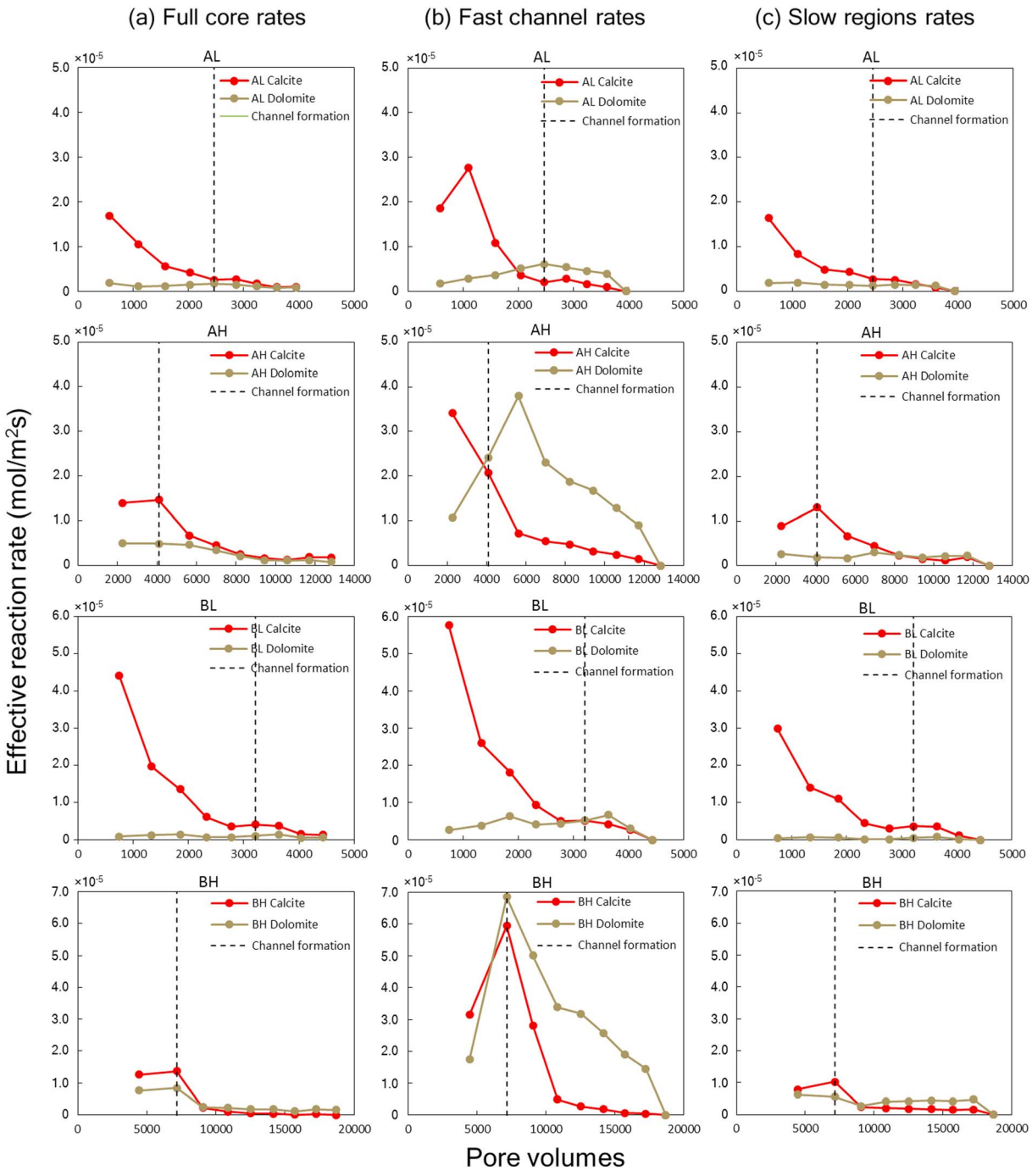

Figure 12. Calcite and dolomite effective reaction rates calculated from the change in mineral volumes in micro-CT images plotted as a function of pore volumes injected. The columns represent the effective rates associated with the surface area related to (a) the full volume, (b) fast channels and (c) slow regions.

and B, which became an order of magnitude lower after approximately 3,000 PV were injected. The same magnitude of reaction rate decrease is observed for the higher flow rate experiments after approximately 9,000 PV for both heterogeneities A and B. At the time when the single channel is formed, the effective reaction rate of calcite and dolomite either decreased considerably (for high flow rates) or were already very low. The dolomite effective reaction rates were slow and steady showing little change in the lower flow rate experiments, while they were initially faster with a later-stage order of magnitude decrease after approximately 9,000 PV in the higher flow rate experiments. At this point, for the BH sample, there was a

crossover of the calcite and dolomite reaction rates, with the dolomite rate exceeding that of calcite. To explain this, we examine the effective reaction rates of calcite and dolomite in fast channels and slow regions.

The analysis of fast channel reaction rates reveals that once the fast channel was formed, the dolomite reacted faster than the calcite, which confirms that calcite was shielded by dolomite. Large remaining regions of calcite are prevented from being in contact with fresh acidic brine by an order of magnitude lower reacting dolomite. The calcite then predominantly reacted in slow regions. For the BH sample both slow regions and fast channel dolomite reaction rates were higher than that of calcite—this resulted in the crossover in the effective reaction rates of calcite and dolomite. This crossover cannot be fully explained by the initial or evolving velocity field heterogeneity, since in single-mineralogy experiments higher flow heterogeneity resulted in lower effective reaction rates due to less efficient transport (Al-Khulaifi et al., 2018). This phenomenon can be attributed to the nonuniform distribution of chemical heterogeneity—in the BH sample most of reacted calcite mineral was initially far away from fast channels, which facilitated dolomite dissolution both in fast channels and slow regions. Changes in pH are unlikely to be the cause of the increasing dolomite reaction rate because the core is sufficiently short that for high velocities (high Pe), the reactant is refreshed rapidly in the fast flow channels. The evolution of reacted calcite and dolomite in relation to fast channels and slow regions will be analyzed in sections 3.2.3 and 3.3.

3.2.3. Spatial Distribution of Reacted Minerals

Next, we examine the changes in spatial distributions of reacted minerals. As seen in Figures 13 and 14, in the more homogeneous samples A many flow channels existed initially, supplying fresh reactant throughout the sample volume to both calcite and dolomite. Hence, we observe significant dissolution of both calcite and dolomite until the single channel is formed. In AL, the formation of the channel was mostly influenced by the preexisting pathways which initiated channel formation by dissolving a cluster of dolomite at the inlet of the core. Due to nonuniform mineral distribution, small amounts of scattered calcite dissolved early but this was not sufficient to influence the formation of the dominant channel. The main flow channel was formed principally through the dissolution of dolomite. From Figures 13 and 14, we observe the single channel formation for both samples A occurred after several thousand PV. Once the channel was formed, fresh reactant flowed through this preferential path, leaving most of the remaining calcite unavailable for reaction since it was shielded by the larger amount of dolomite. Therefore, the effective reaction rate of calcite dropped significantly, while the dolomite rate decreased by a smaller extent.

In the more heterogeneous B samples, shown in Figures 15 and 16, fewer flow channels existed initially, which reduced the availability of fresh reactant throughout the sample volume. Therefore, the initial reaction rate for calcite was lower than those in the less heterogeneous samples A, while at the same time the initial reaction rates for dolomite were higher for the B samples. Visualization of reacted minerals in sample BL shows that only a part of the single channel formed from initially existing channels. The other part of the channel was formed by reaction with initially distant calcite and/or dolomite. For sample BH the entirety of the single dominant channel was formed by the reaction away from the preexisting fast channels. This means that the impact of chemical heterogeneity was more significant than that of physical heterogeneity. This observation shows that transport and reaction should be considered as coupled phenomena, which is the main idea for our analysis in the next section.

3.3. Coupled Transport and Reaction Metrics

3.3.1. Reacted Mineral Proximity to Fast Channels and Slow Regions

In section 2.4 we characterized the initial state of the samples in terms of physical heterogeneity by their initial velocity distributions. To couple the effect of flow and reaction in this section, we study histograms of the proximity of reacted mineral voxels to fast channels and slow regions. In Figures 17–20 we plot the histograms of the proximity of calcite and dolomite voxels that dissolve as a function of their distance from fast channels and slow regions during the period between two experimental scans. The number of voxels are normalized by dividing by the surface area of each mineral in contact with the pore space of the fast channels and slow regions at the end of each experimental scan.

As discussed in section 3.2.3, for more homogeneous A samples, initially many channels existed which supplied fresh reactant throughout the volume resulting in significant contributions to overall dissolution by the calcite in proximity to both fast and slow regions, as seen in Figures 17 and 18. The contribution of calcite

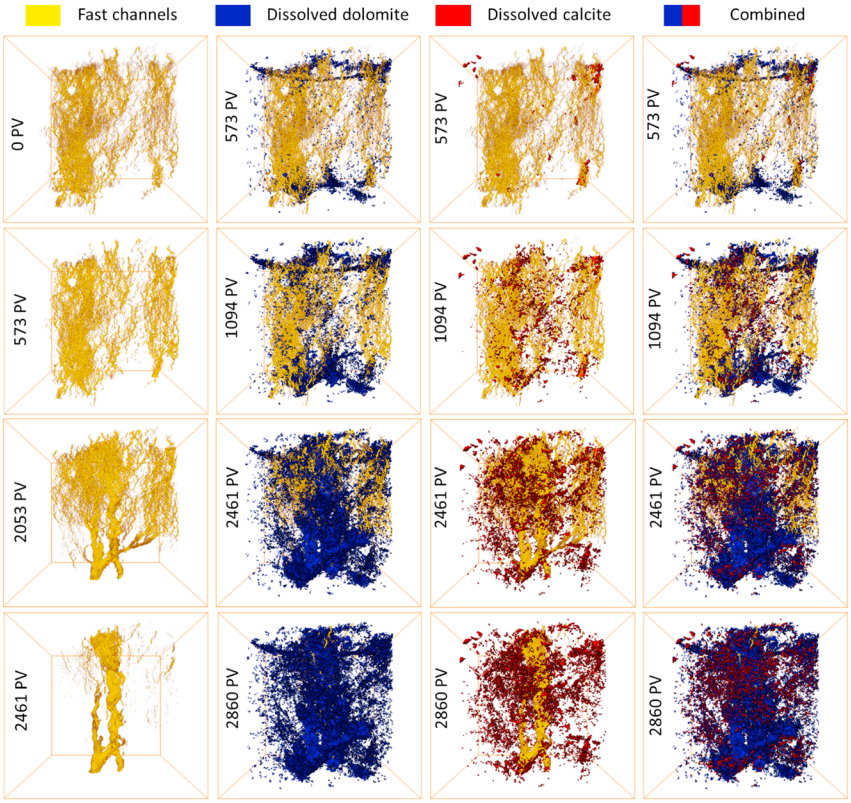

Figure 13. Time lapsed images of fast channels with dissolved calcite and dolomite superimposed for sample AL.

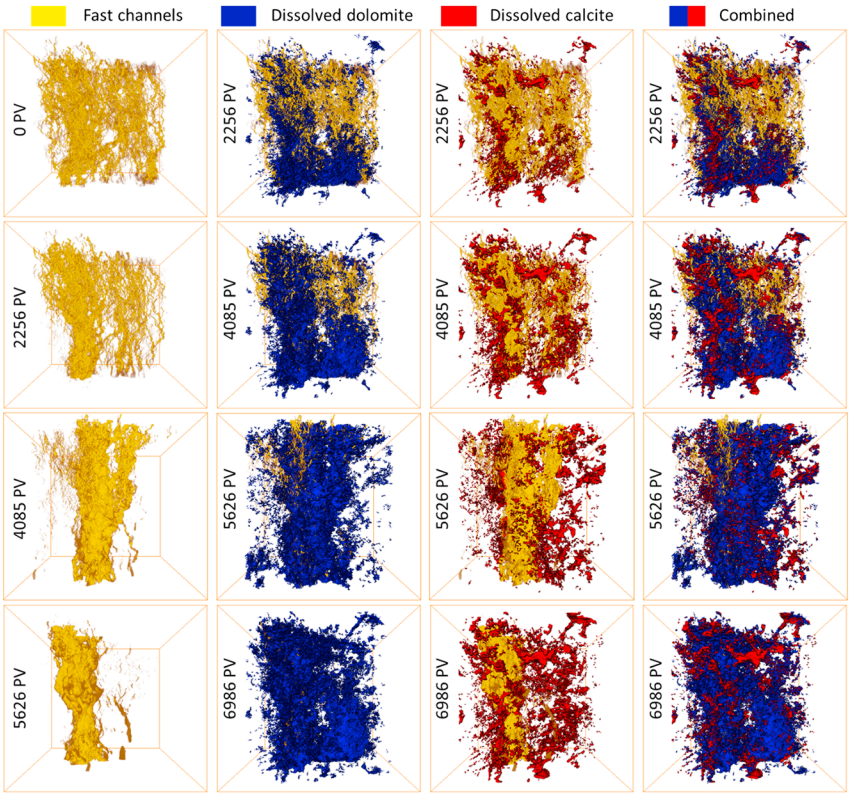

Figure 14. Time lapsed images of fast channels with dissolved calcite and dolomite superimposed for sample AH.

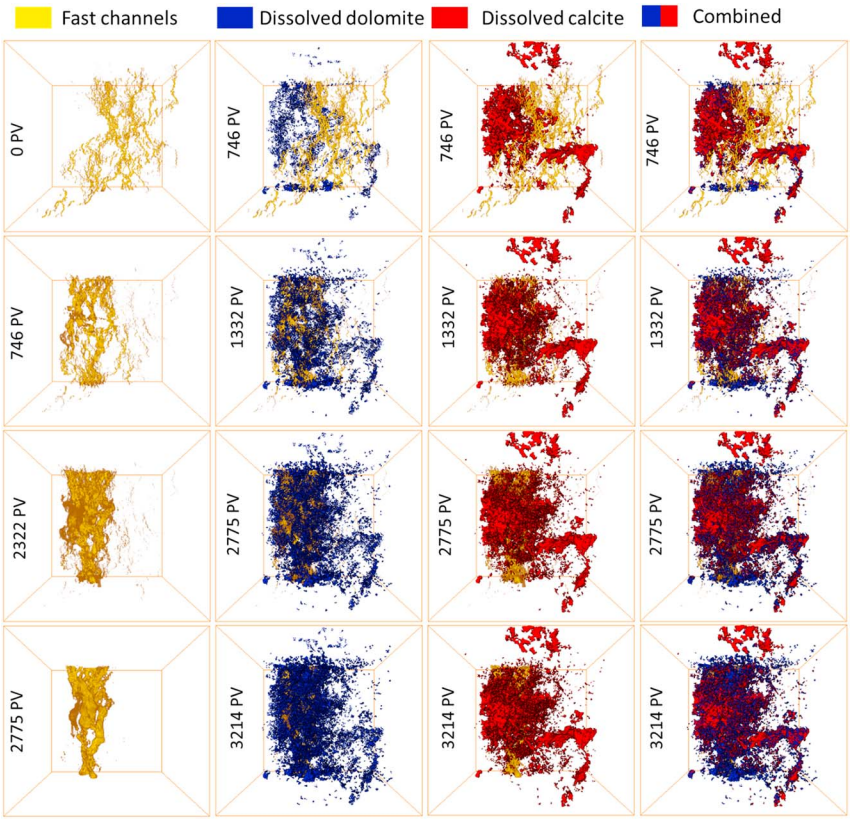

Figure 15. Time lapsed images of fast channels with dissolved calcite and dolomite superimposed for sample BL.

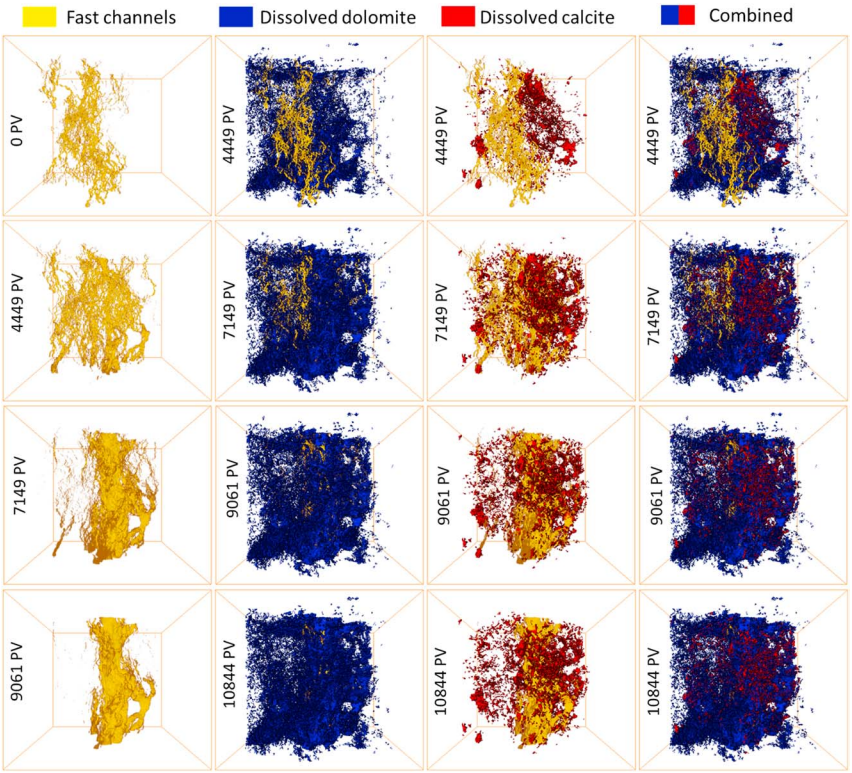

Figure 16. Time lapsed images of fast channels with dissolved calcite and dolomite superimposed for sample BH.

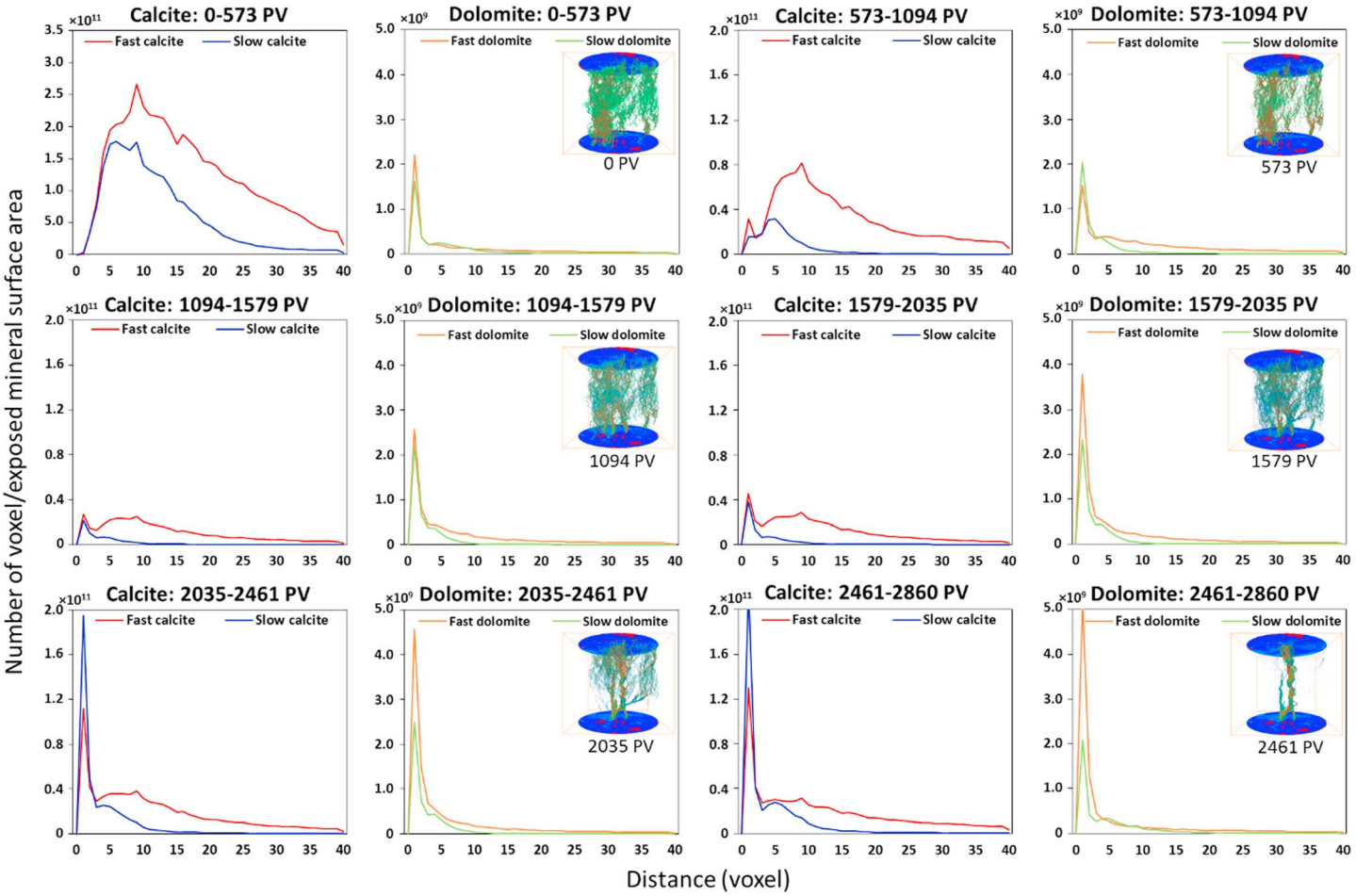

Figure 17. AL sample analysis of dissolution. The dissolved mineral voxels divided by the exposed surface area are shown as a function of distance from either a fast channel or a slow region. Results are shown for different pore volumes (PV) injected for calcite and dolomite and for fast channels and slow regions. Visualization of the flow fields is provided for the beginning of each scan and shown as an insert in the dolomite figures.

dissolution in proximity to the fast flow channels was larger than that near the slow regions until the single channel was formed (for AL experiment this occurred within 2,035–2,461 PV injected, and for AH within 4,085–5,626 PV injected, see Table B2 in Appendix B). From then on, the contribution of calcite dissolution in proximity to the slow regions became more important. However, the opposite is observed for dolomite—since single channel formation resulted in a preferential flow path of fresh reactant, while the mineralogical composition in the channel and the entire sample (see Table B2 in Appendix B and Figure 11) favored dolomite dissolution, we see an increase in the contribution of dolomite dissolution in proximity to the fast flow channels. The dolomite in contact with the single channel prevented the contact of reactant with calcite elsewhere in the rock, thereby further decreasing the calcite effective reaction rate, as shown in Figure 12. This effect is also evident for sample AH in which a larger number of PV were injected after formation of the single channel.

We discriminate different behavior for the higher initial flow heterogeneity samples with heterogeneity B, as seen in Figures 19 and 20. Since they had initially fewer fast flow channels, the supply of fresh reactant was limited to only a part of the sample volume. Hence, initially the contribution of calcite dissolution in proximity to the slow regions was larger than that near the fast channels before the single channel was formed (for BL experiment this occurred within 1,332–1,850 PV injected, and for BH within 7,149–9,061 PV injected, see Table B2). This behavior is also seen after the formation of the preferential flow path, but with much less dissolution and lower calcite effective reaction rates, as previously discussed for the heterogeneity A samples.

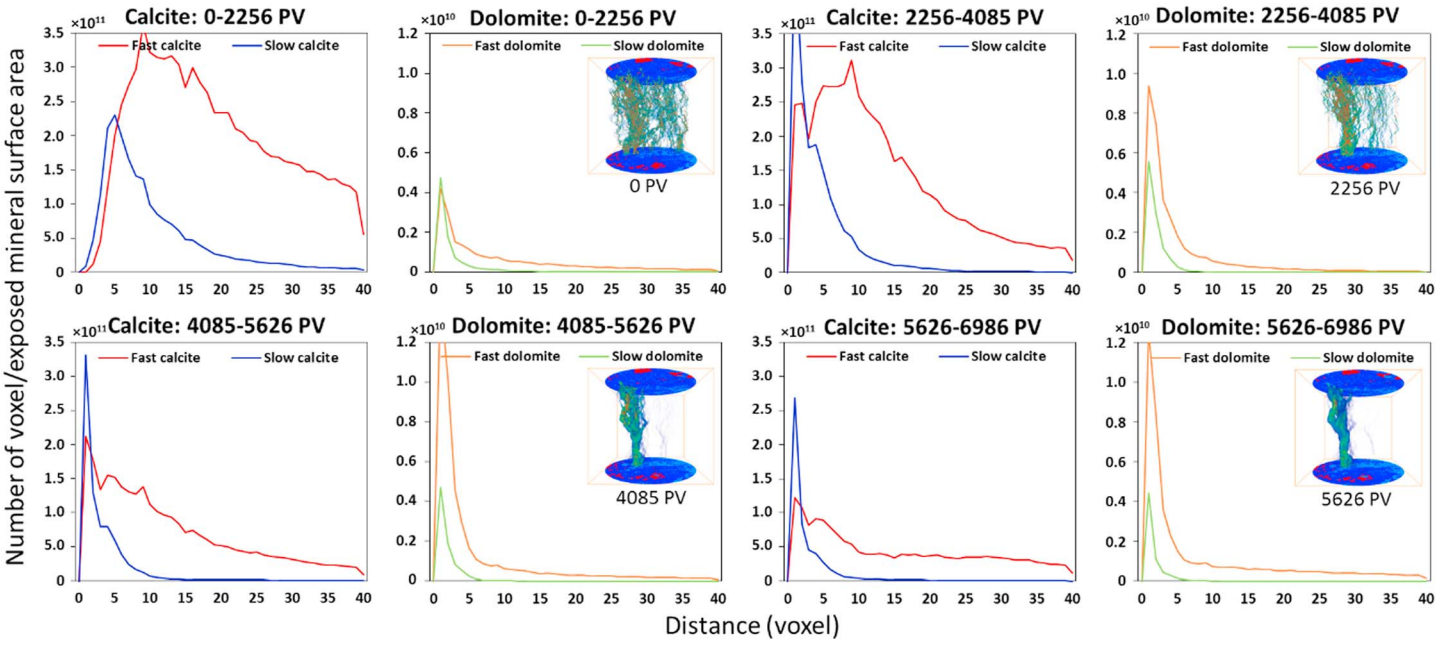

Figure 18. AH sample analysis of dissolution. The dissolved mineral voxels divided by the exposed surface area are shown as a function of distance from either a fast channel or a slow region. Results are shown for different pore volumes (PV) injected for calcite and dolomite, and for fast channels and slow regions. Visualization of the flow fields are provided for the beginning of each scan and shown as an insert in the dolomite figures.

For the B samples the contribution of dolomite dissolution in proximity to the slow flow regions was larger than that near the fast flow channels before the single channel was formed. However, after the formation of the single channel the opposite was true since the preferential flow path of the fresh reactant and mineralogical composition in the channel favored dolomite dissolution.

A larger number of dissolved calcite voxels close to slow regions is a signature that the single channel (BH sample) or parts of it (BL sample) can be formed away from the initially fast channels. This phenomenon is favored by a more heterogeneous flow field (higher probability that initial calcite will be distributed away from the fast channels) and by an order of magnitude higher calcite intrinsic reaction rate than that of dolomite.

4. Conclusions and Implications

We have examined the impact of physical heterogeneity, chemical heterogeneity, and flow rate on the nature of mixed-mineralogy rock dissolution by supercritical CO_2 saturated brine. To reduce the parameter space, we used the SPIM method introduced in Al-Khulaifi et al. (2018) to select two pairs of samples of different heterogeneity in accordance with their initial velocity distributions, for which we then performed experiments at low and high flow rates. The mineralogical composition of the samples was similar (dolomite to calcite ratio of 8:1), but the intrinsic reaction rates of the minerals at the reservoir conditions studied differed by an order of magnitude.

For all the samples studied, visualization of both the velocity field and the reacted mineral distribution revealed that a single dominant flow channel was formed, which considerably decreased the effective reaction rate of calcite as it became shielded by dolomite. However, the formation time and the spatial position of the channel depended on both initial physical and chemical heterogeneity. The more homogeneous samples were characterized by a narrower velocity distribution and a larger number of fast channels throughout the sample volume. This results in the dominant flow pathway being formed from the preexisting flow channels which widened and merged during dissolution. On the other hand, higher pore-structure heterogeneity translates to a broader distribution of velocity and fewer fast channels, which were limited to a part of the sample volume. Here calcite was not necessarily close to fast channels. Hence, calcite dissolution that formed the single dominant channel occurred away from the initially fast channels. This slowed down the formation of single channel. Chemical heterogeneity dominated over physical heterogeneity in these

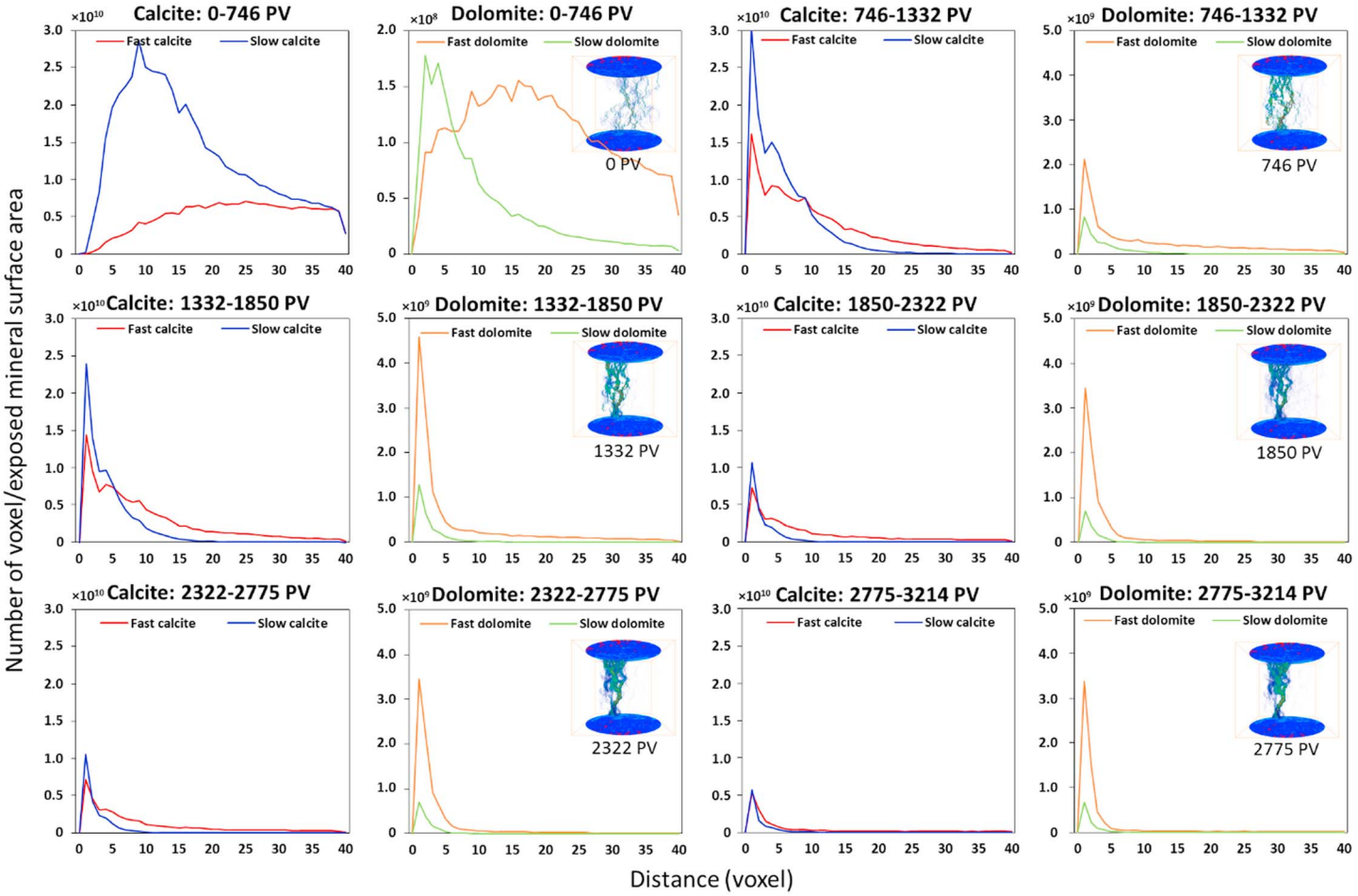

Figure 19. BL sample analysis of dissolution. The dissolved mineral voxels divided by the exposed surface area are shown as a function of distance from either a fast channel or a slow region. Results are shown for different pore volumes (PV) injected for calcite and dolomite, and for fast channels and slow regions. Visualization of the flow fields is provided for the beginning of each scan and shown as an insert in the dolomite figures.

cases. One of the main advantages offered by our methodology is the ability to relate physical and chemical heterogeneity for any pore and mineral distributions. By introducing the functions characterizing the proximity of minerals to fast channels and slow regions reactive transport behavior of any given sample can be generalized in terms of expected effective reaction rates and dissolution patterns.

The average reaction rates calculated over the course of the experiments were at least an order of magnitude lower than the intrinsic reaction rates due to mass transfer limitations. Moreover, the effective reaction rate of calcite decreased due to the establishment of a single preferential flow path. This decrease was much higher than that observed for dolomite, and, dependent on proximity of reacted minerals to fast flow channels, could even lead to a higher effective reaction rate for dolomite than calcite. We explain this behavior by showing that effective rates for dolomite in both fast channels and slow regions were faster than those for calcite, due to the coupled effects of transport heterogeneity and nonuniform mineral distribution.

Our work implies that physical and chemical heterogeneity needs to be added to our traditional picture of reactive transport in porous media. Golfier et al. (2002) plotted Damköhler versus Péclet number graphs to help identify reactive transport conditions needed for the establishment of different dissolution regimes, namely compact (face) dissolution, wormholing, and uniform dissolution. These plots are successfully used for homogenous single mineralogy media but are more limited in describing multimineral porous media where many more reactants are present and for which the definition of Damköhler numbers is not straightforward (Deng et al., 2016). In our pore-scale experiments, the Damköhler numbers (10^{-3}–10^{-4} for calcite, and 10^{-5}–10^{-6} for dolomite) and Péclet numbers (Pe ~ 1,000 for the high flow rate experiment and Pe ~ 100

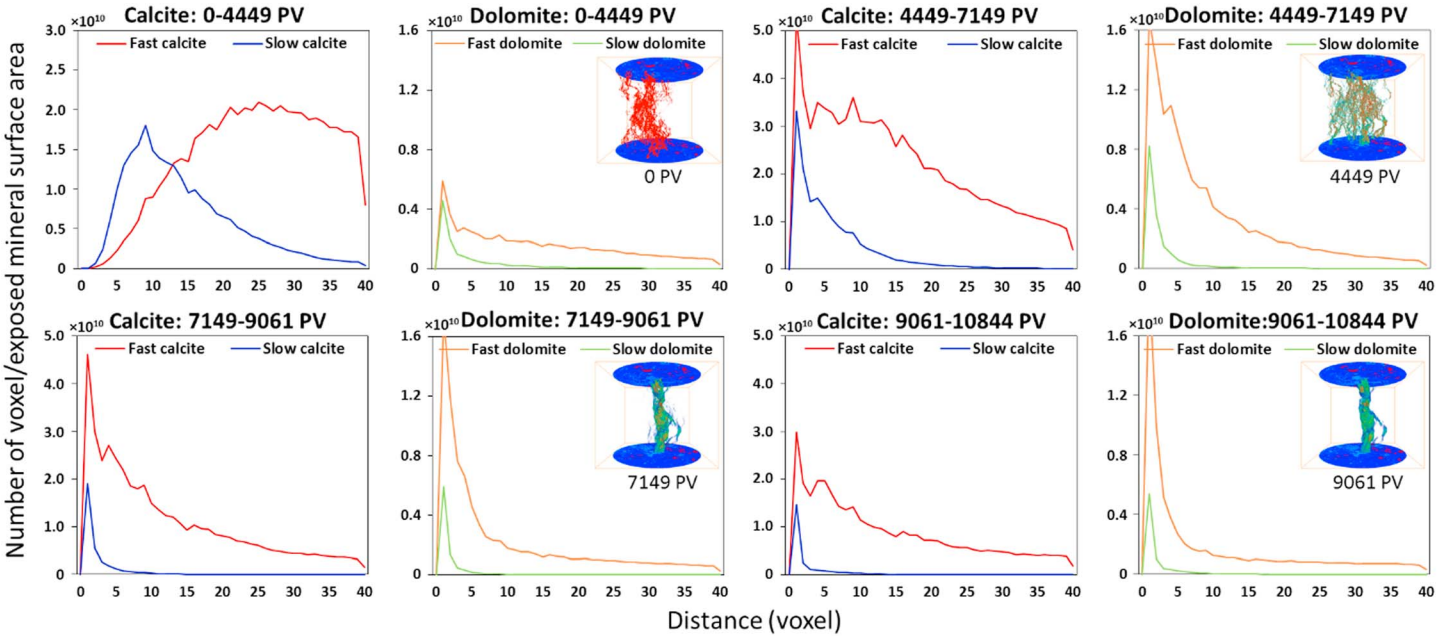

Figure 20. BH sample analysis of dissolution. The dissolved mineral voxels divided by the exposed surface area are shown as a function of distance from either a fast channel or a slow region. Results are shown for different pore volumes (PV) injected for calcite and dolomite and for fast channels and slow regions. Visualization of the flow fields are provided for the beginning of each scan and shown as an insert in the dolomite figures.

for the low flow rate experiment) are in the range of conditions associated with the uniform dissolution regime, as defined by Golfier et al. (2002).

However, the impact of physical heterogeneity leads to a channeling effect, that is, widening of preexisting channels instead of uniform dissolution, as observed in the pore-scale experiments in single-mineralogy experiments (Al-Khulaifi et al., 2018; Menke et al., 2016). Furthermore, our study in multimineral porous media demonstrates that new aspects related to both physical and chemical heterogeneity of porous media should always be considered. Figure 21 illustrates schematically our results: an increase in physical heterogeneity (defined by the velocity distribution) and chemical heterogeneity (defined by the spatial distribution of minerals) leads to preferential channeling, with a decrease in effective reaction rate and a greater scaling exponent in the porosity-permeability relationship.

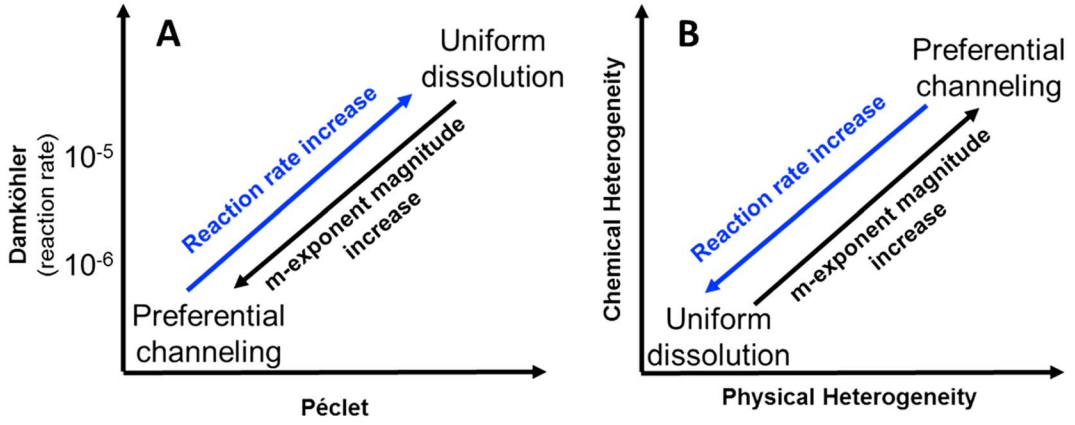

Figure 21. Observed trends in pore-scale dissolution. (a) The general observed trends of pore-scale dissolution at different Péclet and Damköhler numbers and b the impact of physical and chemical heterogeneity in multimineral porous media. An increase in physical and/or chemical heterogeneity is associated with favoring a preferential channeling regime instead of uniform dissolution. This results in the effective reaction rate decrease and a greater scaling exponent m in porosity-permeability power law relationship, $K = c\phi^{m}_{\text{connected}}$.

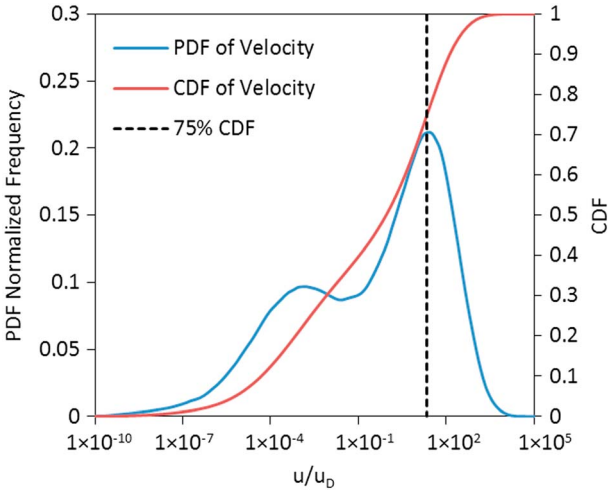

Figure A1. Probability density function (PDF; labels in primary axis) and cumulative density function, CDF (labels on secondary axis) of velocity for the initial flow field of sample BL. The vertical dotted line cuts the CDF trend at the 0.75 CDF, and all velocities above that point are those chosen as the seed to locate channels in the flow field.

Appendix A: Method for Determining the Reacted Mineral Proximity to Fast Channels and Slow Regions

We obtain histograms of distance maps showing the frequency of dissolved calcite and dolomite minerals layer-by-layer away from fast channels and slow regions. The layer thickness is one voxel. Fast channels are identified as those containing velocities that are in the highest 25% of a particular flow field. The algorithm is as follows:

1. Define fast channels in a velocity field
   a. To find the fast velocity *seed* within a particular image we determine the cumulative density function of velocity of the calculated flow field from that image and choose the voxel velocity that corresponds to cumulative density function of 0.75 as the cutoff point. All velocities above that are included in the seed from which to locate a channel. In other words, we segment out the pore voxels with the top 25% of highest velocities (Figure A1).

An example image used for extracting the geometry of fast channels is shown in Figure A2 in which the seeded fast voxels are marked in red in the channel cross section.

   b. We grow the seed (segmented voxels with fastest velocities) to identify the channel volume that contains the fastest velocities. This is done in two steps: (1) using a dilation module in our image analysis software, we grow the seed for a certain number of layers after which there is an insignificant change in the channel volume. In our analysis of the four carbonate samples the number of layers varied between two and eight, dependent on the channel volume. These layers are seen as green in Figure A2b and consist of void and also the solid voxels for which dilated voxels exceeded the pore wall boundary, and (2) if the voxels exceed the pore wall boundary we subtract the solid grain voxels and thus obtain the exact geometry of the channel, which now contains the fastest seed voxels (red) and the voxels with velocity lower than the seed voxels (yellow), as seen in Figure A2c.

2. Define slow regions: subtract the fast channel image acquired in the previous step from the original full image to provide the slow regions.
3. Calculate the number of dissolved calcite and dolomite voxels adjacent to fast channels and slow regions layer by layer moving outward from pore:
   a Step 1: Calculate two distance maps: one that gives the distance of all calcite and dolomite voxels from the outer walls of fast channels and one from the outer walls of slow regions.
   b Step 2: Separate the dissolved calcite and dolomite voxels between two consecutive segmented images using the fast channel and slow regions maps produced in Step 1.
   c Step 3: Make histogram of resulting distance maps to assess the frequency of dissolved calcite and dolomite voxels layer-by-layer away from fast channels and slow regions.

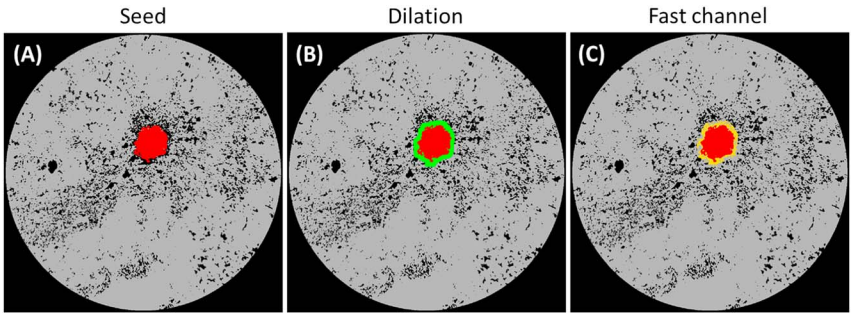

Figure A2. Steps for extracting fast channels: (a) the high velocity voxels (in red), which are used as the seeds; the rock grain voxels are in gray while black voxels are pores, (b) the dilated seeds (in green) in the form of layers covering the fast channel and the adjacent solid grains, and (c) yellow voxels represent the void voxels remaining as part of the channel after removing the solid grain voxels from the dilated voxels in (b).

Appendix B: Summary of Physical and Chemical Parameters Describing Dissolution

Tables B1 and B2 summarize the key observations from the analysis based on the chemical and physical parameter values describing dissolution for the four experimental samples.

Table B1
Interpretation of Results Related to Physical Parameters for Each Sample

Sample	Initial porosity	Final porosity	Initial permeability	Final permeability	Velocity field	Velocity distribution
AL	9.9%	15.3%	7.6×10^{-15} m^2	5.3×10^{-11} m^2	Initially, many fast channels existed; calcite and dolomite dissolved along the initial fast flow channels leading to channel widening	A secondary peak developed where the channel was formed; previously fast velocity peak became slower relative to the secondary peak.
AH	11.3%	21.4%	5.0×10^{-14} m^2	8.0×10^{-10} m^2	Initially, many fast channels existed; calcite and dolomite dissolved along the initial fast flow channels leading to channel widening	A secondary peak developed and was higher than the AL case (as the channel is wider); correspondingly less of previously high velocities became more stagnant relative to the secondary peak
BL	7.9%	13.0%	1.7×10^{-15} m^2	3.7×10^{-11} m^2	Fewer channels initially made the dissolution of calcite away from fast channels more probable	Secondary peak formed, while the primary peak moved toward stagnant velocities relative to the secondary peak
BH	8.0%	18.0%	2.3×10^{-15} m^2	4.7×10^{-10} m^2	Fewer channels initially made the dissolution of calcite away from fast channels more probable	New secondary peak was very pronounced because of calcite dissolution, while the initial peak moved toward stagnant velocities relative to the secondary peak

Table B2
Interpretation of Results Related to Chemical Parameters for Each Sample

Sample	Initial dol. and cal. content (vol%)	Final dol. and cal. content (vol%)	PV needed to form the channel	Effective reaction rates	Mineral distribution	Reacted mineral proximity to fast channel
AL	Dol:81.5% Cal: 8.7%	Dol:77.0% Cal: 7.7%	2,035–2,461	Dolomite reaction rate was low and steady; calcite reaction rate decreased but never crossed over dolomite rate	Calcite and dolomite dissolved throughout the sample volume until the single dominant channel was formed	Reacted calcite was initially in the proximity of fast channels due to the homogeneous initial flow field
AH	Dol:78.4% Cal: 10.3%	Dol:70.0% Cal: 8.6%	2,256–4,085	Dolomite rate was initially higher than in the A low flow rate case; calcite reaction rate had a decreasing trend but never crossed over dolomite rate	Calcite and dolomite dissolved throughout the sample volume until the single dominant channel was formed	Reacted calcite was initially in the proximity of fast channels due to the homogeneous initial flow field
BL	Dol:79.7% Cal: 12.4%	Dol:77.4% Cal: 9.6%	2,775–3,214	Dolomite rate was low and steady; calcite reaction rate initially very high and decreased with time, but never crossed over dolomite rate	Part of the single dominant channel was from the preexisting channel; however, the other part of the channel was from a distant calcite	Reacted calcite was initially away from fast channels due to the heterogeneous initial flow field
BH	Dol:84.6% Cal: 7.3%	Dol:76.2% Cal: 5.8%	4,449–7,149	Dolomite rate was initially higher than in the B low flow rate case; calcite reaction rate was high and decreased until it crosses over dolomite rate at 9,000 PV	The entirety of the single dominant channel was formed away from initially fast channels	Reacted calcite was initially away from fast channels due to the heterogeneous initial flow field

Note. PV = pore volumes. Dol. represents dolomite, and Cal. represents calcite.

Acknowledgments

We gratefully acknowledge funding from the Qatar Carbonates and Carbon Storage Research Centre (QCCSRC), provided jointly by Qatar Petroleum, Shell, and Qatar Science and Technology Park. The segmented images used in this study can be downloaded from https://doi.org/10.5285/52b08e7f-9fba-40a1-b0b5-dda9a3c83be2.

References

Al-Khulaifi, Y., Lin, Q., Blunt, M. J., & Bijeljic, B. (2017). Reaction rates in chemically heterogeneous rock: Coupled impact of structure and flow properties studied by X-ray microtomography. *Environmental Science and Technology*, *51*(7), 4108–4116. https://doi.org/10.1021/acs.est.6b06224

Al-Khulaifi, Y., Lin, Q., Blunt, M. J., & Bijeljic, B. (2018). Reservoir-condition pore-scale imaging of dolomite reaction with supercritical CO_2 acidified brine: Effect of pore-structure on reaction rate using velocity distribution analysis. *International Journal of Greenhouse Gas Control*, *68*, 99–111. https://doi.org/https://doi.org/10.1016/j.ijggc.2017.11.011

Bachu, S. (2000). Sequestration of CO_2 in geological media: Criteria and approach for site selection in response to climate change. *Energy Conversion and Management*, *41*(9), 953–970. https://doi.org/10.1016/S0196-8904(99)00149-1

Beisman, J. J., Maxwell, R. M., Navarre-Sitchler, A. K., Steefel, C. I., & Molins, S. (2015). ParCrunchFlow: An efficient, parallel reactive transport simulation tool for physically and chemically heterogeneous saturated subsurface environments. *Computational Geosciences*, *19*(2), 403–422. https://doi.org/10.1007/s10596-015-9475-x

Bijeljic, B., Mostaghimi, P., & Blunt, M. J. (2013). Insights into non-Fickian solute transport in carbonates. *Water Resources Research*, *49*, 2714–2728. https://doi.org/10.1002/wrcr.20238

Bijeljic, B., Raeini, A., Mostaghimi, P., & Blunt, M. J. (2013). Predictions of non-Fickian solute transport in different classes of porous media using direct simulation on pore-scale images. *Physical Review E - Statistical, Nonlinear, and Soft Matter Physics*, *87*(1), 13,011. https://doi.org/10.1103/PhysRevE.87.013011

Black, J. R., Carroll, S. A., & Haese, R. R. (2015). Rates of mineral dissolution under CO_2 storage conditions. *Chemical Geology*, *399*(0, 134–144. https://doi.org/10.1016/j.chemgeo.2014.09.020

Celia, M. A., Bachu, S., Nordbotten, J. M., & Bandilla, K. W. (2015). Status of CO_2 storage in deep saline aquifers with emphasis on modeling approaches and practical simulations. *Water Resources Research*, *51*, 6846–6892. https://doi.org/10.1002/2015WR017609

Deng, H., Molins, S., Steefel, C., DePaolo, D., Voltolini, M., Yang, L., & Ajo-Franklin, J. (2016). A 2.5D reactive transport model for fracture alteration simulation. *Environmental Science & Technology*, *50*(14), 7564–7571. https://doi.org/10.1021/acs.est.6b02184

Deng, H., Steefel, C., Molins, S., & DePaolo, D. (2018). Fracture evolution in multimineral systems: The role of mineral composition, flow rate, and fracture aperture heterogeneity. *ACS Earth and Space Chemistry*, *2*(2), 112–124. https://doi.org/10.1021/acsearthspacechem.7b00130

Ellis, B., Peters, C., Fitts, J., Bromhal, G., McIntyre, D., Warzinski, R., & Rosenbaum, E. (2011). Deterioration of a fractured carbonate caprock exposed to CO_2-acidified brine flow. *Greenhouse Gases: Science and Technology*, *1*(3), 248–260. https://doi.org/10.1002/ghg.025

Gharbi, O., Bijeljic, B., Boek, E. S., & Blunt, M. J. (2013). Changes in pore structure and connectivity induced by CO_2 injection in carbonates: A combined pore-scale approach. *Energy Procedia*, *37*(0, 5367–5378. https://doi.org/10.1016/j.egypro.2013.06.455

Golfier, F., Zarcone, C., Bazin, B., Lenormand, R., Lasseux, D., & Quintard, M. (2002). On the ability of a Darcy-scale model to capture wormhole formation during the dissolution of a porous medium. *Journal of Fluid Mechanics*, *457*, 213–254. https://doi.org/10.1017/S0022112002007735

Gouze, P., & Luquot, L. (2011). X-ray microtomography characterization of porosity, permeability and reactive surface changes during dissolution. *Journal of Contaminant Hydrology*, *120–121*(C), 44–55. https://doi.org/10.1016/j.jconhyd.2010.07.004

Hao, Y., Smith, M., Sholokhova, Y., & Carroll, S. (2013). CO2-induced dissolution of low permeability carbonates. Part II: Numerical modeling of experiments. *Advances in Water Resources*, *62*, 388–408. https://doi.org/10.1016/j.advwatres.2013.09.009

Li, L., Peters, C. A., & Celia, M. A. (2006). Upscaling geochemical reaction rates using pore-scale network modeling. *Advances in Water Resources*, *29*(9), 1351–1370. https://doi.org/10.1016/j.advwatres.2005.10.011

Li, L., Salehikhoo, F., Brantley, S. L., & Heidari, P. (2014). Spatial zonation limits magnesite dissolution in porous media. *Geochimica et Cosmochimica Acta*, *126*, 555–573. https://doi.org/10.1016/j.gca.2013.10.051

Li, L., Steefel, C. I., & Yang, L. (2008). Scale dependence of mineral dissolution rates within single pores and fractures. *Geochimica et Cosmochimica Acta*, *72*(2), 360–377. https://doi.org/10.1016/j.gca.2007.10.027

Luquot, L., & Gouze, P. (2009). Experimental determination of porosity and permeability changes induced by injection of CO_2 into carbonate rocks. *Chemical Geology*, *265*(1–2), 148–159. https://doi.org/10.1016/j.chemgeo.2009.03.028

Maheshwari, P., Ratnakar, R. R., Kalia, N., & Balakotaiah, V. (2013). 3-D simulation and analysis of reactive dissolution and wormhole formation in carbonate rocks. *Chemical Engineering Science*, *90*(0, 258–274. https://doi.org/10.1016/j.ces.2012.12.032

Marty, N. C. M., Bildstein, O., Blanc, P., Claret, F., Cochepin, B., Gaucher, E. C., et al. (2015). Benchmarks for multicomponent reactive transport across a cement/clay interface. *Computational Geosciences*, *19*(3), 635–653. https://doi.org/10.1007/s10596-014-9463-6

Menke, H., Andrew, M. G., Blunt, M. J., & Bijeljic, B. (2016). Reservoir condition imaging of reactive transport in heterogeneous carbonates using fast synchrotron tomography—Rffect of initial pore structure and flow conditions. *Chemical Geology*, *428*, 15–26. https://doi.org/10.1016/j.chemgeo.2016.02.030

Menke, H., Bijeljic, B., Andrew, M. G., & Blunt, M. J. (2015). Dynamic three-dimensional pore-scale imaging of reaction in a carbonate at reservoir conditions. *Environmental Science and Technology*, *49*(7), 4407–4414. https://doi.org/10.1021/es505789f

Menke, H., Bijeljic, B., & Blunt, M. J. (2017). Dynamic reservoir-condition microtomography of reactive transport in complex carbonates: Effect of initial pore structure and initial brine pH. *Geochimica et Cosmochimica Acta*, *204*, 267–285. https://doi.org/10.1016/j.gca.2017.01.053

Menke, H., Reynolds, C. A., Andrew, M. G., Pereira Nunes, J. P., Bijeljic, B., & Blunt, M. J. (2018). 4D multi-scale imaging of reactive flow in carbonates: Assessing the impact of heterogeneity on dissolution regimes using streamlines at multiple length scales. *Chemical Geology*, *481*, 27–37. https://doi.org/10.1016/J.CHEMGEO.2018.01.016

Metz, B., Davidson, O., De Coninck, H., Loos, M., & Meyer, L. (2005). IPCC special report on carbon dioxide capture and storage. Prepared by working group III of the Intergovernmental Panel on Climate Change. In *IPCC Special Report on Carbon Dioxide Capture and Storage* (Vol. 2, p. 442). https://doi.org/10.1002/anie.201000431

Molins, S., Trebotich, D., Steefel, C. I., & Shen, C. (2012). An investigation of the effect of pore scale flow on average geochemical reaction rates using direct numerical simulation. *Water Resources Research*, *48*, W03527. https://doi.org/10.1029/2011WR011404

Moore, J., Lichtner, P. C., White, A. F., & Brantley, S. L. (2012). Using a reactive transport model to elucidate di ff erences between laboratory and field dissolution rates in regolith. *Geochimica et Cosmochimica Acta*, *93*, 235–261. https://doi.org/10.1016/j.gca.2012.03.021

Morse, J. W., & Mackenzie, F. T. (1990). *Geochemistry of sedimentary carbonates, developments in sedimentology* (Vol. 48). Amsterdam, Netherlands: Elsevier. https://doi.org/10.1016/S0070-4571(08)70330-3

Mostaghimi, P., Bijeljic, B., & Blunt, M. (2012). Simulation of flow and dispersion on pore-space images. *SPE Journal*, *17*, 1131–1141. https://doi.org/10.2118/135261-PA

Noiriel, C., Bernard, D., Gouze, P., & Thibault, X. (2005). Hydraulic properties and microgeometry evolution accompanying limestone dissolution by acidic water. *Oil and Gas Science and Technology*, *60*(1), 177–192. https://doi.org/10.2516/ogst:2005011

Noiriel, C., Gouze, P., & Bernard, D. (2004). Investigation of porosity and permeability effects from microstructure changes during limestone dissolution. *Geophysical Research Letters*, *31*, L24603. https://doi.org/10.1029/2004GL021572

Noiriel, C., Luquot, L., Madé, B., Raimbault, L., Gouze, P., & van der Lee, J. (2009). Changes in reactive surface area during limestone dissolution: An experimental and modelling study. *Chemical Geology*, *265*(1-2), 160–170. https://doi.org/10.1016/j.chemgeo.2009.01.032

Peng, C., Anabaraonye, B. U., Crawshaw, J. P., Maitland, G. C., & Trusler, J. P. M. (2016). Kinetics of carbonate mineral dissolution in CO_2-acidified brines at storage reservoir conditions. *Faraday Discussions*, *192*, 545–560. https://doi.org/10.1039/c6fd00048g

Peng, C., Crawshaw, J. P., Maitland, G. C., Martin Trusler, J. P., & Vega-Maza, D. (2013). The pH of CO_2-saturated water at temperatures between 308K and 423K at pressures up to 15MPa. *The Journal of Supercritical Fluids*, *82*, 129–137. https://doi.org/10.1016/j.supflu.2013.07.001

Peng, C., Crawshaw, J. P., Maitland, G. C., & Trusler, J. P. M. (2015). Kinetics of calcite dissolution in CO_2-saturated water at temperatures between (323 and 373)K and pressures up to 13.8MPa. *Chemical Geology*, *403*(0, 74–85. https://doi.org/10.1016/j.chemgeo.2015.03.012

Raeini, A. Q., Blunt, M. J., & Bijeljic, B. (2012). Modelling two-phase flow in porous media at the pore scale using the volume-of-fluid method. *Journal of Computational Physics*, *231*(17), 5653–5668. https://doi.org/10.1016/j.jcp.2012.04.011

Salehikhoo, F., & Li, L. (2015). The role of magnesite spatial distribution patterns in determining dissolution rates: When do they matter? *Geochimica et Cosmochimica Acta*, *155*, 107–121. https://doi.org/10.1016/j.gca.2015.01.035

Sifuentes, W., Blunt, M. J., & Giddins, M. a. (2009). Modeling CO_2 storage in aquifers: Assessing the key contributors to uncertainty. SPE Offshore Europe Oil & Gas Conference & Exhibition, (July), SPE123582. https://doi.org/10.2118/123582-MS

Smith, M. M., Hao, Y., & Carroll, S. A. (2017). Development and calibration of a reactive transport model for carbonate reservoir porosity and permeability changes based on CO_2 core-flood experiments. *International Journal of Greenhouse Gas Control*, *57*, 73–88. https://doi.org/https://doi.org/10.1016/j.ijggc.2016.12.004

Smith, M. M., Hao, Y., Mason, H. E., & Carroll, S. A. (2014). Experiments and modeling of variably permeable carbonate reservoir samples in contact with CO_2-acidified brines. *Energy Procedia*, *63*, 3126–3137. https://doi.org/10.1016/j.egypro.2014.11.337

Smith, M. M., Sholokhova, Y., Hao, Y., & Carroll, S. A. (2013). CO_2-induced dissolution of low permeability carbonates. Part I: Characterization and experiments. *Advances in Water Resources*, *62*, 370–387. https://doi.org/10.1016/j.advwatres.2013.09.008

Steefel, C. I., Appelo, C. A. J., Arora, B., Jacques, D., Kalbacher, T., Kolditz, O., et al. (2015). Reactive transport codes for subsurface environmental simulation. *Computational Geosciences*, *19*(3), 445–478. https://doi.org/10.1007/s10596-014-9443-x

Steefel, C. I., Beckingham, L. E., & Landrot, G. (2015). Micro-continuum approaches for modeling pore-scale geochemical processes. *Reviews in Mineralogy and Geochemistry*, *80*(1), 217–246. https://doi.org/10.2138/rmg.2015.80.07

Steefel, C. I., & Lasaga, A. C. (1994). A coupled model for transport of multiple chemical species and kinetic precipitation/dissolution reactions with application to reactive flow in single phase hydrothermal systems. *American Journal of Science*, *294*(5), 529–592. https://doi.org/10.2475/ajs.294.5.529

Steefel, C. I., & Maher, K. (2009). Fluid-rock interaction: A reactive transport approach. *Reviews in Mineralogy and Geochemistry*, *70*(1), 485–532. https://doi.org/10.2138/rmg.2009.70.11

Swoboda-Colberg, N. G., & Drever, J. I. (1993). Mineral dissolution rates in plot-scale field and laboratory experiments. *Chemical Geology*, *105*(1–3), 51–69. https://doi.org/10.1016/0009-2541(93)90118-3

Wang, Y., Hill, A. D., & Schechter, R. S. (1993). The optimum injection rate for matrix acidizing of carbonate formations. Proceedings of SPE Annual Technical Conference and Exhibition. Society of Petroleum Engineers. https://doi.org/10.2523/26578-MS

White, A. F., & Brantley, S. L. (2003). The effect of time on the weathering of silicate minerals: Why do weathering rates differ in the laboratory and field? *Chemical Geology*, *202*(3–4), 479–506. https://doi.org/10.1016/j.chemgeo.2003.03.001